International Journal of Mechanical Sciences 288 (2025) 110023

Contents lists available at ScienceDirect

International Journal of Mechanical Sciences

journal homepage: www.elsevier.com/locate/ijmecsci

Resilient multi-layered lattices with alternating chirality for self-recovering energy absorption

Andrea Bacigalupo, Vito Diana, Luigi Gambarotta *

DICCA, University of Genoa, Italy

ARTICLE INFO

Keywords:
Resilient metamaterials
Self-recovering
Chirality
Energy absorption
Hysteretic response

ABSTRACT

This research focuses on the development of a high-performance metamaterial that combines dissipation and resilience, a subject of growing actual interest in vibration and impact mechanics as part of the quest for avant-garde self-recovering materials. In this context, a high-performance resilient layered metamaterial with alternating chiral topology is conceived and analyzed. Specifically, the single layer is realized via the periodic assembly of rigid disks connected by elastic ligaments and stacked using passing pins. The metadevice is formed by stacking layers with alternating chirality. This configuration induces relative rotations between the aligned discs in contact when in-plane forces are applied. Frictional dilating interfaces between adjacent disks produce a dissipative and resilient mechanical response, returning to the initial configuration at the end of the unloading phase. Specifically, the dissipative mechanism is designed to significantly attenuate vibratory motions and/or absorb energy during impact processes, while being reusable after the dynamic actions have acted on the metamaterial. This cutting-edge metamaterial offers several advantages over current technologies: i) hysteretic response with maximum dissipation of mechanical energy and high stiffness; ii) reuse of the device without external interventions, restoring the initial configuration at the end of the dynamic process; iii) multi-directional dissipative response; and iv) bilateral response, providing equal performance under both traction and compression.

1. Introduction

Resilient energy-absorbing metamaterials are a class of engineered materials that are showing great promise in many technological applications to mitigate shock damage or dampen vibrations. Compared to traditional damping/shock absorbing materials, which base their inelastic response on the viscoelastic properties of amorphous polymers [1–3] or on the plastic deformation and crushing of metal foams [4,5], dissipative metamaterials may achieve a virtuous combination of high damping and high stiffness [6]. Moreover, while viscoelastic materials retain their efficiency at the end of a dynamic process, with the dissipated energy depending on the timescale of load application, materials undergoing plastic deformation and crushing perform better but are not reusable after an energy absorption event. Various micro-architected materials with mechanical energy absorption capacity have been proposed in the literature, supported by advancements in additive manufacturing techniques (see for instance [7]).

Several micro-architected metamaterials have been proposed, with energy absorption systems primarily dependent on the destructive modification of their microstructure [8–10]. Examples include periodic metallic honeycombs [11], various types of metallic microlattices [12–16], ceramic nanolattices [17], hierarchical architected metamaterials [18], chiral microlattices [7], viscoelastic metastructures made with elastomeric polymers [19], patterned thin-walled meta--structures [8], shape memory alloys [20] to name a few.

Micro-structured periodic materials designed to trap elastic strain energy through metastable periodic cell assemblies have been proposed and tested by several scholars. Some microstructures exhibit force-displacement performance of the unit cell tailored to create self-recovering materials, which return to their original configuration after each energy absorption event, or reusable but non-self-recovering materials, where the deformed microstructure must be actively restored. However, in most cases, materials that are reusable but not self-recovering have been developed, requiring active intervention to return the deformed metamaterial to its original configuration. Periodic micro-structured materials were proposed in [21], featuring a representative cell composed of bistable tilted beams that switch to an alternate stable configuration, exhibiting hysteresis during loading and

* Corresponding author.
E-mail address: luigi.gambarotta@unige.it (L. Gambarotta).

https://doi.org/10.1016/j.ijmecsci.2025.110023
Received 13 August 2024; Received in revised form 27 January 2025; Accepted 27 January 2025
Available online 31 January 2025

unloading, with elastic reversibility of the transformation. Reusable, self-recovering energy-absorbing materials with periodic microstructural cells formed by sinusoidal beams acting as elastic bistable or metastable mechanisms were proposed and tested in [22,23]. In addition, an extensive theoretical analysis of the characteristics of mechanical metamaterials based on snap-through elements, including the behaviour of a finite number of unstable elements, was conducted [24]. In this context, several lattices with varying cell topologies have been proposed to maximise energy dissipation while ensuring reusability and, where possible, self-recovery of the devices [25–31]. In [32], architected materials with tunable shear behaviour and high energy dissipation have been proposed, while in [33] a shear-induced, multi-stable dissipative metamaterial featuring magnet systems arranged periodically within the microstructure has been developed. Recent proposals for three-dimensional microstructured materials include cells made of multistable disks and conical shells [34,35], as well as lattices [36–40], aimed at achieving reusable energy-absorbing materials. In this context, the properties of chiral topological lattices with multistable cells are particularly relevant for designing reusable and self-recovering energy-absorbing materials. Moreover, lattices with chiral cells composed of bistable tape springs that connect rotating and translating disks have been proposed and analyzed in [41]. Following this, a periodic microstructure with unit cells that undergo a series of stable configurations, derived from the sequential insertion of the plug into the groove of the snap-fit in the cell, was proposed in [42]. These mechanisms are a source of energy dissipation under compression and ensure the reusability of the system. A similar dissipative material was developed in [43], where a self-recoverable negative stiffness metamaterial with enhanced bearing and energy dissipation capacity was achieved through mutual extrusion and friction between a snap plug and a layered snap groove. The metamaterial proposed in [44] combined bistable behaviour with friction-based elements to achieve remarkable damping properties. A new unit cell was designed, incorporating both a spring and a snap-fit element. A similar approach was followed in [45], where a two-phase material cell system incorporating a multistable device resulted in a reusable dissipative system. In [46], a two-layer metamaterial was proposed, with each layer featuring an identical pattern but opposite chirality (see [47]), designed to achieve relative rotation between aligned nodes controlled by a multistable elasto-magnetic device. Numerical simulations conducted by the authors revealed significant energy dissipation under normal stresses and limited energy absorption under shear stresses

An alternative approach to developing new metamaterials for reusable and/or self-recovering energy absorption involves coupling self-tensioning stretchable components with frictional devices that dissipate energy. In this context, it is important to highlight that this technique has recently been extended to the structural level to design dissipative and reusable structural elements in [48–50], and its bio-inspired nature has been demonstrated in [51]. A metamaterial was proposed and tested in [52], where repeated unit cells combine rigid granular materials with frictional interactions and compliant stretchable components, designed to achieve bistability or multistability. Simple experiments demonstrated that, for certain configurations of granules and elastic components, exceptional energy absorption and self-recovery could be achieved. In this regard, it is important to note that designing microstructures capable of accommodating displacement discontinuities between internal surfaces in contact within the periodic cell—controlled by appropriate passive or active mechanical (e.g., frictional) or electromechanical devices—may be particularly useful for achieving dissipative and self-recovering material behaviours. A metamaterial was developed in [53], where the periodic cells are designed to trigger internal Coulombic frictional sliding between contact surfaces of elastic components strategically positioned within the cell when subjected to uniaxial loading and unloading, enabling repeatable energy dissipation. Several unit cells were designed with a central arrow-shaped feature and two cantilevered legs that contact and bend against the arrow under load. As the legs bend, contact force increases and the arrow's sliding motion relative to the legs generates frictional dissipation. The experimental response of single cells and cell groups to pulsating uniaxial compression showed a stable, trilinear behaviour, exhibiting notable energy dissipation and self-recovery—i.e., unloading to the undeformed state at the end of each cycle—resembling the behaviour of micro-cracked materials with internal friction (see, for example [54]). An analogous frictional metamaterial was proposed in [55], consisting of a central hexagonal or re-entrant honeycomb frame, a lower section with four tapered columns, and an upper portion with a blade shape. The metamaterial is characterized by remarkable energy dissipation and stiffness under compressive stress. A friction-based energy-dissipating metamaterial for bidirectional loading was adopted in [56]. Their design incorporates a periodic cell with two orthogonal axes of symmetry, consisting of four spirals and straight walls that create a gap between each spiral's inner tip and the boundary wall. At low compressive forces, this compliant structure facilitates frictional sliding between internal surfaces once a certain axial displacement is reached, enabling energy dissipation and full self-recovery at the end of each loading-unloading cycle. A dissipative, self-centering metamaterial under compression was proposed in [57], with a unit cell designed to generate significant frictional forces. The load applied to the edge of the unit cell is redirected to its interior, utilizing a mechanism similar to the re-entrant honeycomb structure to produce lateral contraction under compressive forces. This contraction generates a normal force on the frictional sliding surfaces within the structure, thereby controlling the compression along the direction of the externally applied force. A new family of 3D tiled auxetic metamaterials demonstrating remarkable resilience under large deformations and significant hysteresis under cyclic compressive loading was proposed in [58]. A space-filling tessellation of octahedrons and cuboctahedrons is connected through devices with tailored elastic-frictional behavior. The metamaterial is characterized by notable energy dissipation and self-recoverability under compression. A micro-structured material incorporating a friction-based energy dissipation mechanism was introduced in [59,60]. This integration enhances both the effective stiffness and the auxetic effect. The response of both the unit cell and its periodic assembly to compressive stress exhibits a hysteretic, self-centering behavior, characterized by limited stiffness and moderate energy dissipation.

Despite these significant contributions, the challenge of identifying the optimal microstructure to achieve the following performance criteria remains open: (i) a hysteretic response with maximum mechanical energy dissipation and stiffness; (ii) reusability of the device without external intervention, allowing it to return to its initial configuration after the dynamic process; (iii) multi-directional dissipative response; and (iv) bilateral response, with symmetrical behavior under both tension and compression.

This study tackles the challenge by proposing a resilient metamaterial that fulfills these requirements. An energy-absorbing layered metamaterial, composed of repeated lattices with alternating chiral topologies and a periodic arrangement of rigid disks connected by elastic ligaments, is proposed. The rotational mechanism observed in chiral lattices [61–65] inspired the development of novel three-dimensional metamaterials, achieved by layering chiral lattices with alternating chirality. This configuration induces relative rotations between disks in adjacent layers, controlled by frictional interactions that facilitate energy dissipation. A similar simplified model was proposed in [66], based on a micropolar description of the layers. The material response was analyzed under the assumptions of a homogeneous displacement gradient and uniform rotation, deriving the model's behavior within the framework of a standard Cauchy continuum. The layered metamaterial is described in greater detail through a discrete Lagrangian model, relaxing the assumption of transverse rigidity of the pins and adopting a frictional-dilatant interface model. This approach enables the treatment of more general biaxial tension/compression states and facilitates the evaluation of its dissipative properties, which are found to be

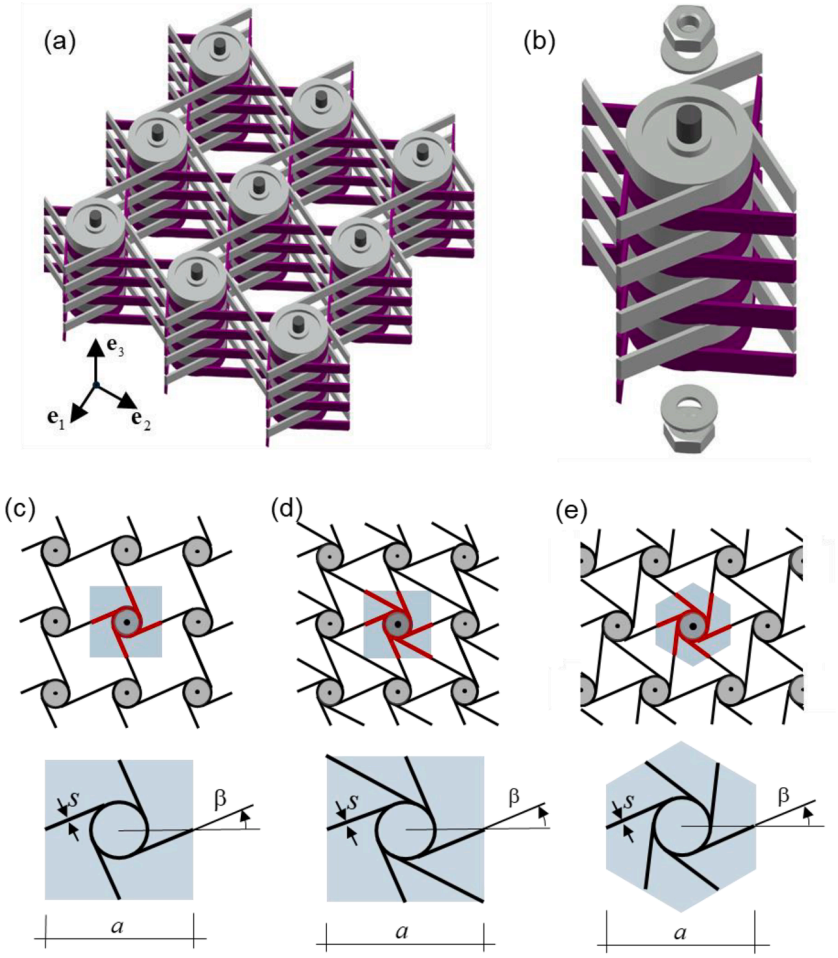

Fig. 1. View of the metamaterial and considered chiral topologies: (a) portion of hexachiral layer; (b) a portion of the stratified medium; (c) tetrachiral lattice; (d) square-based hexachiral lattice; (e) regular hexachiral lattice.

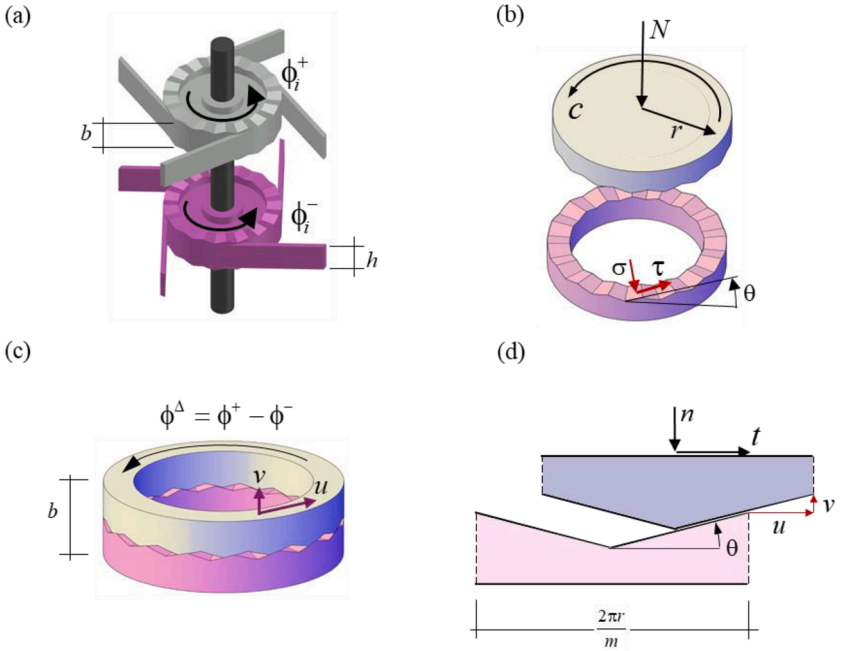

Fig. 2. The interface between adjacent disks: (a) detail of the dilatant interface between disks of two contiguous layers; (b) the interaction generalized forces between the disks; (c) dilatant mechanism is governed by the relative rotation between the disks and displacements at the points of contact between the disks; (d) detail of the dilatant mechanism associated with an interface tooth.

exceptional, confirming that the model's response meets the required specifications. Several examples are discussed, from which the properties of the model and its limits of validity can be deduced.

2. The energy dissipating multi-layered metamaterials with alternating chirality

The proposed energy-absorbing metamaterial is based on internal frictional devices formed by a layered assembly of periodic lattices having alternating chirality (Fig. 1a). Each layer consists of a periodic arrangement of rigid disks of thickness b, connected by m slender, straight elastic ligaments of length ℓ and rectangular cross-section $s \times h$ (see Fig. 2a). The lattice features a chiral topology (Fig. 1), defined by the angle β between each ligament and the line connecting the centers of adjacent disks, as shown in Fig. 1c-e for lattices with positive chirality ($\beta > 0$). The peculiarity of these lattices lies in the rotational response of the disks when overall tractions are applied, with the direction of rotation depending on the sign of the chirality [61–64].

The stratified system is assembled using elastic pins that pass through the aligned discs and are secured at the ends with appropriate nuts, as shown in Fig. 1b. Once in-plane boundary displacements or forces are uniformly applied along the thickness of the metamaterial (unit vector $\mathbf{e}_3$), relative rotations between the disks of adjacent layers with opposite chirality can occur [47]. The disks are designed to rotate freely around the pins. Consequently, the relative rotation between the disks is controlled by the interaction couples between the disks themselves, which are governed by friction. Frictional tractions between the contact surfaces of adjacent disks are generated by compressing the disks orthogonally to their plane, an effect achieved when the pins are subjected to tension. In this model, the traction of the pins is obtained by superimposing the initial traction N_0, achieved by appropriately tightening the nuts at the ends of the pins, with the additional traction generated by the dilatant mechanism associated with the relative rotation between the disks, which is based on the sawtooth interface shown in Fig. 2.

The traction of the pin can be written as $N = N_0 + N_{\Delta\phi}$, where the second term is linearly related to the transverse dilation $\varepsilon_3 = \frac{v}{b}$ in the form $N_{\Delta\phi} = E_p A_p \varepsilon_3$, E_p and A_p being the elastic modulus and the cross-section of the pin, respectively. In the mechanical model under consideration, friction effects are assumed to arise from the relative rotations between the discs, while relative displacements are disregarded, as they are negligible (as demonstrated in Section 4.2). From the kinematic model in Fig. 2d, it follows that the vertical component of the relative displacement $v = u\tan\theta$ depends on the angle θ of inclination of the teeth of the interface. Here $u = \phi^{\Delta} r$ is the relative displacement between two contacting disks and depends on their relative rotation ϕ^{Δ} and r the radius of the circle relative to which the system description is referenced (see Fig. 2b). The axial force $N = N_0 + E_p A_p \frac{r}{b} \tan\theta \phi^{\Delta}$ turns out to be the compressive force acting on the disks and can be evenly distributed among m portions of the disk, where m is the total number of teeth. If the m-th portion is considered (see Fig. 2d) the compressive force per unit length of the reference circle is $n = N/2\pi r$, while the corresponding tangential force, resulting from the interface couple c, is expressed as $t = c/2\pi r^2$. If the contact configuration at incipient infinitesimal sliding is considered, as illustrated in Fig. 2d, and it is assumed that the contact tractions σ and τ defined on the reference circle are uniform along the contact line (see Fig. 2b), the following relationships can be derived from equilibrium

$$\begin{aligned} \sigma &= 2n\cos^2\theta + 2t\sin\theta\cos\theta, \\ \tau &= -2n\sin\theta\cos\theta + 2t\cos^2\theta. \end{aligned} \tag{1}$$

If the friction limit state à la Coulomb $\varphi(\sigma,\tau) = |\tau| - f\sigma \le 0$ is assumed, being f the friction coefficient, the plastic-attritive admissibility condition governing the relative rotation between the disks and the interface couple c can be expressed in the following form

$$\begin{aligned} \varphi^*(c,\phi^{\Delta},N_0) \quad = \quad & |c - (N_0 r + k\tan\theta\phi^{\Delta})\tan\theta| + \\ & -f[c\tan\theta + (N_0 r + k\tan\theta\phi^{\Delta})] \le 0 \end{aligned} \tag{2}$$

which depends on the interface couple c, the relative rotation between the discs ϕ^{Δ}, the initial axial force N_0 applied on the pin and the constant $k = \frac{E_p A_p r^2}{b}$. It can be observed that in case of plane interfaces, namely $\theta = 0$, then the plastic-attritive admissibility condition takes the form of perfect plasticity

$$\widehat{\varphi}(c,N_0) = |c| - fN_0 r \le 0. \tag{3}$$

These are two actions that can be accomplished independently. In the scenario where only pre-tensioning of the pins is active, with no asperities at the interfaces ($\theta = 0$), a highly dissipative system is achieved depending on the friction coefficient. However, this system can only be reset for reuse by releasing the pre-tensioning through unscrewing the nuts.

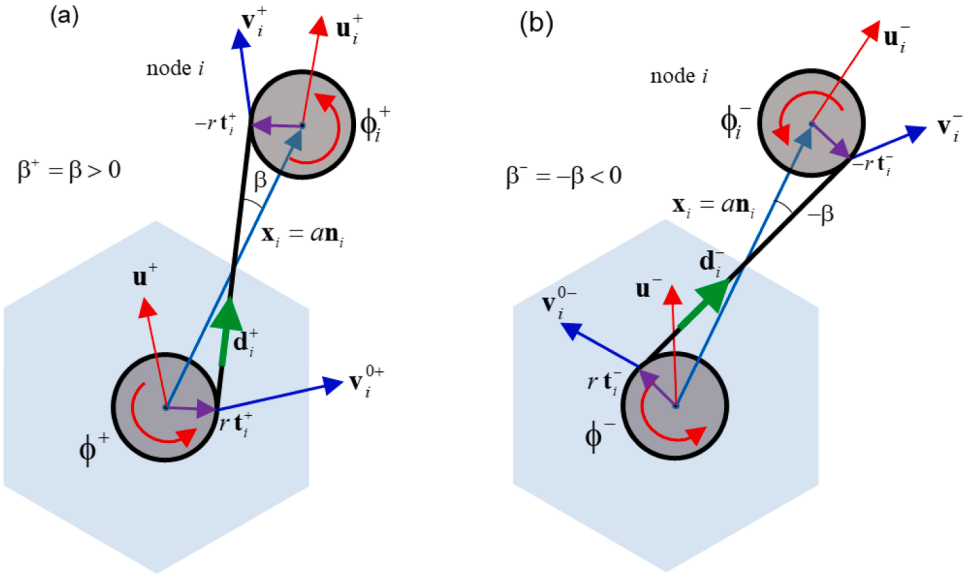

Fig. 3. Kinematics of adjacent nodes for opposite chirality: (a) detail of the dilatant interface between disks of two contiguous layers; (b) dofs of the reference periodic cell and those the i-th adjacent one.

In the case of saw-tooth interfaces with frictional contact and no pretension, it will be shown that relative rotation, denoted as ϕ^{Δ}, occurs at the beginning of the load history. As the relative rotation increases, the axial force in the pin also increases due to the dilatancy effect, thereby enhancing the frictional couple. In this scenario, a dissipative response is achieved, as it will be shown in Section 4.1. However, upon removal of the applied external forces, the metamaterial returns to its initial configuration, as demonstrated in the case of homogeneous deformations by Bacigalupo *et al.* [66], thereby highlighting its self-centering and reusability properties.

3. The discrete Lagrangian model

From the description of the layered metamaterial provided in Section 2, a discrete Lagrangian model can be defined as described below. The periodic structure of the layers along the $\mathbf{e}_3$ direction (see Fig. 1a) and from the assumption of periodicity of the generalized forces acting on the layers imply the periodicity of the in-plane displacements and rotations of the rigid disks stacked along the generic h-th pin (h being the pin label, $h = 1,..,N$) labelled as $\mathbf{u}_h^+$, $\mathbf{u}_h^-$, ϕ_h^+ and ϕ_h^- referred to the layer having positive and negative chirality, respectively, as shown in Fig. 2a (in the following the superscript + or – denote the positive and negative chirality layer).

A discrete Lagrangian micro-mechanical model having six in-plane degrees of freedom for each node may be formulated. If the average and difference state variable defined through the *average* operator $\overline{\bullet} = \frac{1}{2}(\bullet^+ + \bullet^-)$ and the *difference* operator $\bullet^{\Delta} = \bullet^+ - \bullet^-$ are introduced (see also [66,67]), so implying the *inverse* operators $\bullet^{\pm} = \overline{\bullet} \pm \frac{1}{2}\bullet^{\Delta}$, the Lagrangian function referred to the periodic layer of thickness $2b$ and composed by two adjacent layers having positive and negative chirality may be introduced

$$\mathscr{L} = \mathrm{A}_{h=1}^{N}\left\{\begin{array}{l} T(\dot{\overline{\mathbf{u}}}, \dot{\mathbf{u}}^{\Delta}, \dot{\overline{\phi}}, \dot{\phi}^{\Delta}) - \sum_{i=1}^{m}\Pi_i(\overline{\mathbf{u}}, \mathbf{u}^{\Delta}, \overline{\phi}, \phi^{\Delta}, \overline{\mathbf{u}}_i, \mathbf{u}_i^{\Delta}, \overline{\phi}_i, \phi_i^{\Delta}) + \\ -\Pi_p(\mathbf{u}^{\Delta}) - \mathscr{V}(\overline{\mathbf{u}}, \mathbf{u}^{\Delta}, \overline{\phi}, \phi^{\Delta}) \end{array}\right\}, \tag{4}$$

where the symbol $A_{h=1}^{N}$ denotes the properly defined operator assembling the contributions of all the N nodes, the sum is extended to the m ligaments connecting the reference disk (m being the coordination number), $(\overline{\mathbf{u}}, \mathbf{u}^{\Delta}, \overline{\phi}, \phi^{\Delta})$ denotes the average and difference generalized displacement of the reference h-th node, while $(\overline{\mathbf{u}}_i, \mathbf{u}_i^{\Delta}, \overline{\phi}_i, \phi_i^{\Delta})$ the generalized displacements of the node connected through the i-th ligament (see Fig. 3a,b).

The contribution to the total kinetic energy of the two disks centred at the reference node is

$$T(\dot{\overline{\mathbf{u}}}, \dot{\mathbf{u}}^{\Delta}, \dot{\overline{\phi}}, \dot{\phi}^{\Delta}) = M\dot{\overline{\mathbf{u}}}\cdot\dot{\overline{\mathbf{u}}} + \frac{1}{4}M\dot{\mathbf{u}}^{\Delta}\cdot\dot{\mathbf{u}}^{\Delta} + I\dot{\overline{\phi}}^2 + \frac{1}{4}I(\dot{\phi}^{\Delta})^2, \tag{5}$$

with M and J the mass and the polar inertia of the disk, respectively. The potential of the generalized forces acting on the referred disk may be written in the form

$$\mathscr{V}(\overline{\mathbf{u}}, \mathbf{u}^{\Delta}, \overline{\phi}, \phi^{\Delta}) = -2\overline{\mathbf{f}}\cdot\overline{\mathbf{u}} - \frac{1}{2}\mathbf{f}^{\Delta}\cdot\mathbf{u}^{\Delta} - 2\overline{m}\overline{\phi} - \frac{1}{2}m^{\Delta}\phi^{\Delta}, \tag{6}$$

where $\overline{\mathbf{f}}$, $\mathbf{f}^{\Delta}$, $\overline{m}$, m^{Δ} are the average and difference of the forces and couples applied to the disks, respectively, with periodic distribution along the thickness. The disks aligned along a pin interact through two separate contact regions. The first interaction between two adjacent disks takes place through the contact forces acting on the pin. Since the pin is designed to behave elastically with no frictional interaction with the disks, its effect may be synthetically described through the shear elastic potential energy

$$\Pi_p(\mathbf{u}^{\Delta}) = \frac{1}{2}K_p(\mathbf{u}^+ - \mathbf{u}^-)^2 = \frac{1}{2}K_p(\mathbf{u}^{\Delta})^2, \tag{7}$$

K_p being the shear stiffness of the pin. Vice versa, the contact forces acting on the lateral surfaces of adjacent disks have a plastic/frictional character, i.e. are source of energy dissipation, and are synthetically described in terms of interaction couples denoted as c^+ and c^-, respectively. Thus, following Podio Guidugli and Virga [67] and Hackl *et al.* [68], a Rayleigh-like dissipation function can be introduced

$$R(\dot{\phi}^+, \dot{\phi}^-) = 2c^+\dot{\phi}^+ + 2c^-\dot{\phi}^- = 4\overline{c}\dot{\overline{\phi}} + c^{\Delta}\dot{\phi}^{\Delta} = R^*(\dot{\overline{\phi}}, \dot{\phi}^{\Delta}). \tag{8}$$

Due to the principle of action and reaction it follows $c^+ + c^- = 2\overline{c} = 0$ and $c^{\Delta} = \frac{1}{2}(c^+ - c^-) = c^+ = c$ so that the contribution of the referred node to the dissipation function takes the following form

$$R(\dot{\overline{\phi}}, \dot{\phi}^{\Delta}) = c^{\Delta}\dot{\phi}^{\Delta} = c\dot{\phi}^{\Delta}. \tag{9}$$

According to Gambarotta and Bacigalupo [65], the contribution to the elastic potential energy due to the axial deformation of the i-th ligament is written in the form (refer to Fig. 3a,b)

$$\Pi_{ai}^{\pm} = \frac{1}{2}\eta_i Eh\left[(\mathbf{u}_i^{\pm} - \mathbf{u}^{\pm})\cdot\mathbf{d}_i^{\pm} - \frac{a}{2}\sin(\pm\beta)(\phi_i^{\pm} + \phi^{\pm})\right]^2, \tag{10}$$

$\eta_i = \frac{s}{l_i}$ being the ratio between the ligament thickness and length, while the contribution due to the ligament bending is

$$\Pi_{bi}^{\pm} = \frac{E_s h s^2 \eta_i}{6}\left\{\begin{array}{l} \left[\phi^{\pm} \pm \frac{1}{l}(\mathbf{u}_i^{\pm} - \mathbf{u}^{\pm})\cdot\mathbf{t}_i^{\pm}\right]^2 + \left[\phi_i^{\pm} \pm \frac{1}{l}(\mathbf{u}_i^{\pm} - \mathbf{u}^{\pm})\cdot\mathbf{t}_i^{\pm}\right]^2 + \\ + \left[\phi^{\pm} \pm \frac{1}{l}(\mathbf{u}_i^{\pm} - \mathbf{u}^{\pm})\cdot\mathbf{t}_i^{\pm}\right]\left[\phi_i^{\pm} \pm \frac{1}{l}(\mathbf{u}_i^{\pm} - \mathbf{u}^{\pm})\cdot\mathbf{t}_i^{\pm}\right] \end{array}\right\}. \tag{11}$$

The Euler-Lagrange equations of motion of the referred disk are derived via variational method after proper manipulations of the Lagrangian and the Rayleigh-like dissipation functions and take the form

$$\left\{\begin{array}{l} 2M\ddot{\overline{\mathbf{u}}} + E\sum_i^m \eta_i h[\mathbf{G}_i(\overline{\mathbf{u}} - \overline{\mathbf{u}}_i) + af_1(\beta)\mathbf{m}_i(\overline{\phi} + \overline{\phi}_i) + af_2(\beta)\mathbf{n}_i(\phi^{\Delta} + \phi_i^{\Delta})] - 2\overline{\mathbf{f}} = \mathbf{0} \\ \frac{M}{2}\ddot{\mathbf{u}}^{\Delta} + E\sum_i^m \eta_i h\left[\frac{\mathbf{G}_i}{4}(\mathbf{u}^{\Delta} - \mathbf{u}_i^{\Delta}) + af_2(\beta)\mathbf{n}_i(\overline{\phi} + \overline{\phi}_i) + a\frac{f_1(\beta)}{4}\mathbf{m}_i(\phi^{\Delta} + \phi_i^{\Delta})\right] + K_p\mathbf{u}^{\Delta} - \frac{\mathbf{f}^{\Delta}}{2} = \mathbf{0} \\ 2I\ddot{\overline{\phi}} + Ea\sum_i^m \eta_i h[f_1(\beta)\mathbf{m}_i\cdot(\overline{\mathbf{u}} - \overline{\mathbf{u}}_i) + f_2(\beta)\mathbf{n}_i\cdot(\mathbf{u}^{\Delta} - \mathbf{u}_i^{\Delta}) + af_3(\beta)(\overline{\phi} + \overline{\phi}_i) + af_4(\beta)\overline{\phi}_i] - 2\overline{m} = 0 \\ \frac{I}{2}\ddot{\phi}^{\Delta} + Ea\sum_i^m \eta_i h\left[f_2(\beta)\mathbf{n}_i\cdot(\overline{\mathbf{u}} - \overline{\mathbf{u}}_i) + \frac{f_1(\beta)}{4}\mathbf{m}_i\cdot(\mathbf{u}^{\Delta} - \mathbf{u}_i^{\Delta}) + a\frac{f_3(\beta)}{4}(\phi^{\Delta} + \phi_i^{\Delta}) + a\frac{f_4(\beta)}{4}\phi_i^{\Delta}\right] - \frac{m^{\Delta}}{2} - c = 0 \end{array}\right., \tag{12}$$

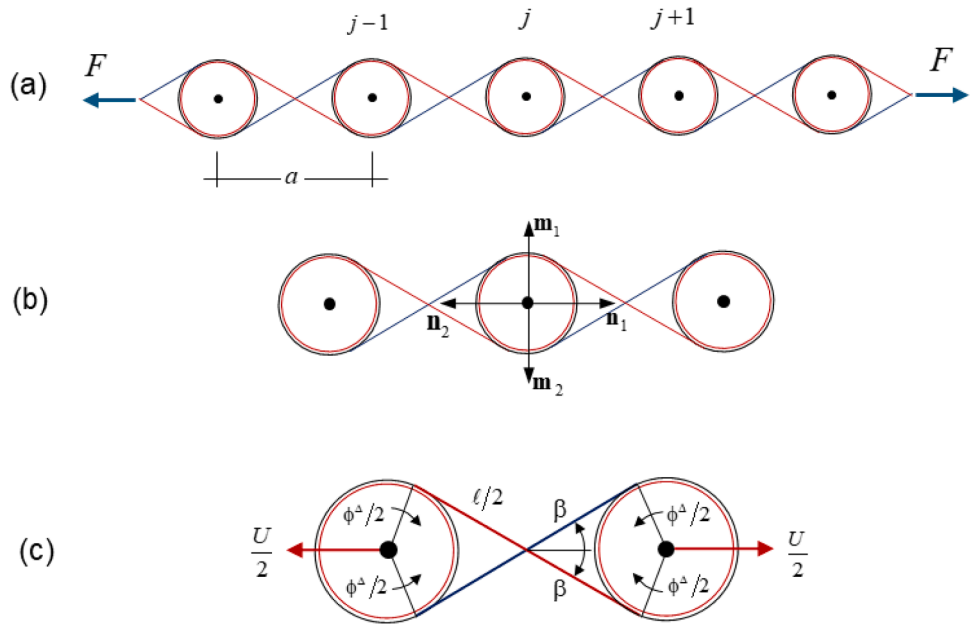

Fig. 4. The tensioned one-dimensional chain: (a) geometry and applied forces; (b) unit vectors characterizing the lattice; (c) kinematics of the disks.

where the auxiliary quantities

$$\begin{aligned}\mathbf{G}_i &= 2\left(\mathbf{D}_i+\eta^2\mathbf{T}_i\right)=2\left(\mathbf{d}_i^+\otimes\mathbf{d}_i^+ +\eta^2\mathbf{t}_i^+\otimes\mathbf{t}_i^+\right)= \\ &= 2\left[\mathbf{R}(\beta)(\mathbf{n}_i\otimes\mathbf{n}_i)\mathbf{R}(\beta)^T+\eta^2\mathbf{R}\left(\beta-\frac{\pi}{2}\right)(\mathbf{n}_i\otimes\mathbf{n}_i)\mathbf{R}\left(\beta-\frac{\pi}{2}\right)^T\right] \\ \mathbf{m}_i &= \mathbf{R}\left(\frac{\pi}{2}\right)\mathbf{n}_i\end{aligned}$$

are introduced in terms of the unit vector $\mathbf{n}_i$ and the in-plane rotation tensor $\mathbf{R}(\cdot)$, as well as the following $\beta-$ dependent functions

$$f_1(\beta)=-\frac{1}{2}\left[1-\eta^2-\left(1+\eta^2\right)\cos(2\beta)\right], f_2(\beta)=\frac{1}{4}\left(1-\eta^2\right)\sin(2\beta),$$

$$f_3(\beta)=\frac{1}{12}\left(3+4\eta^2-\left(3-4\eta^2\right)\cos(2\beta)\right), f_4(\beta)=-\frac{\eta^2}{6}\left(1+\cos(2\beta)\right).$$

By introducing the following macro-vectors collecting the generalized displacements of the N disks, with sub-vectors defined as follows $[\overline{\mathbf{U}}]_h=\overline{\mathbf{u}}_h$, $[\overline{\mathbf{U}}^\Delta]=\mathbf{u}_h^\Delta$, $[\overline{\Theta}]_h=\overline{\phi}_h$, $[\mathbf{\Theta}^\Delta]_h=\phi_h^\Delta$, together with the macro-vectors collecting the applied and internal generalized forces $[\overline{\mathbf{F}}]_h=\overline{\mathbf{f}}_h$, $[\mathbf{F}^\Delta]_h=\mathbf{f}_h^\Delta$, $[\overline{\mathbf{m}}]_h=\overline{m}_h$, $[\mathbf{m}^\Delta]_h=m_h^\Delta$, $[\mathbf{c}]_h=c_h$ and the generalized inertia tensors $\mathbf{M}=M\mathbf{I}_{2M}$, $\mathbf{J}=J\mathbf{I}_M$, $\mathbf{I}_M$, $\mathbf{I}_{2M}$ being identity matrices of order M and $2M$, respectively, the equations of motion (12) of the nodes of the layered material may be rewritten in the compact form

$$\begin{bmatrix}2\mathbf{M}&\mathbf{0}&\mathbf{0}&\mathbf{0}\\ \mathbf{0}&\frac{1}{2}\mathbf{M}&\mathbf{0}&\mathbf{0}\\ \mathbf{0}&\mathbf{0}&2\mathbf{J}&\mathbf{0}\\ \mathbf{0}&\mathbf{0}&\mathbf{0}&\frac{1}{2}\mathbf{J}\end{bmatrix}\begin{Bmatrix}\ddot{\overline{\mathbf{U}}}\\ \ddot{\mathbf{U}}^\Delta\\ \ddot{\overline{\mathbf{\Theta}}}\\ \ddot{\mathbf{\Theta}}^\Delta\end{Bmatrix}+\begin{bmatrix}\mathbf{K}_{\overline{UU}}&\mathbf{0}&\mathbf{K}_{\overline{U\Theta}}&\mathbf{K}_{\overline{U}\mathbf{\Theta}^\Delta}\\ \mathbf{0}&\mathbf{K}_{U^\Delta U^\Delta}&\mathbf{K}_{U^\Delta\overline{\Theta}}&\mathbf{K}_{U^\Delta\mathbf{\Theta}^\Delta}\\ \mathbf{K}_{\overline{\Theta U}}&\mathbf{K}_{\overline{\Theta}U^\Delta}&\mathbf{K}_{\overline{\Theta\Theta}}&\mathbf{0}\\ \mathbf{K}_{\mathbf{\Theta}^\Delta\overline{U}}&\mathbf{K}_{\mathbf{\Theta}^\Delta U^\Delta}&\mathbf{0}&\mathbf{K}_{\mathbf{\Theta}^\Delta\mathbf{\Theta}^\Delta}\end{bmatrix}\begin{Bmatrix}\overline{\mathbf{U}}\\ \mathbf{U}^\Delta\\ \overline{\mathbf{\Theta}}\\ \mathbf{\Theta}^\Delta\end{Bmatrix}$$
$$=\begin{Bmatrix}2\overline{\mathbf{F}}\\ \frac{1}{2}\mathbf{F}^\Delta\\ 2\overline{\mathbf{m}}\\ \frac{1}{2}\mathbf{m}^\Delta+\mathbf{c}\end{Bmatrix}. \tag{13}$$

If the applied generalized forces are uniformly distributed along direction $\mathbf{e}_3$ one obtains $\mathbf{F}^\Delta=\mathbf{0}$ and $\mathbf{m}^\Delta=\mathbf{0}$. Moreover, if no external couple is applied to the disks, one also obtains $\overline{\mathbf{m}}=\mathbf{0}$. In this case, the equations of motion read

$$\begin{bmatrix}2\mathbf{M}&\mathbf{0}&\mathbf{0}&\mathbf{0}\\ \mathbf{0}&\frac{1}{2}\mathbf{M}&\mathbf{0}&\mathbf{0}\\ \mathbf{0}&\mathbf{0}&2\mathbf{J}&\mathbf{0}\\ \mathbf{0}&\mathbf{0}&\mathbf{0}&\frac{1}{2}\mathbf{J}\end{bmatrix}\begin{Bmatrix}\ddot{\overline{\mathbf{U}}}\\ \ddot{\mathbf{U}}^\Delta\\ \ddot{\overline{\mathbf{\Theta}}}\\ \ddot{\mathbf{\Theta}}^\Delta\end{Bmatrix}+\begin{bmatrix}\mathbf{K}_{\overline{UU}}&\mathbf{0}&\mathbf{K}_{\overline{U\Theta}}&\mathbf{K}_{\overline{U}\mathbf{\Theta}^\Delta}\\ \mathbf{0}&\mathbf{K}_{U^\Delta U^\Delta}&\mathbf{K}_{U^\Delta\overline{\Theta}}&\mathbf{K}_{U^\Delta\mathbf{\Theta}^\Delta}\\ \mathbf{K}_{\overline{\Theta U}}&\mathbf{K}_{\overline{\Theta}U^\Delta}&\mathbf{K}_{\overline{\Theta\Theta}}&\mathbf{0}\\ \mathbf{K}_{\mathbf{\Theta}^\Delta\overline{U}}&\mathbf{K}_{\mathbf{\Theta}^\Delta U^\Delta}&\mathbf{0}&\mathbf{K}_{\mathbf{\Theta}^\Delta\mathbf{\Theta}^\Delta}\end{bmatrix}\begin{Bmatrix}\overline{\mathbf{U}}\\ \mathbf{U}^\Delta\\ \overline{\mathbf{\Theta}}\\ \mathbf{\Theta}^\Delta\end{Bmatrix}$$
$$=\begin{Bmatrix}2\overline{\mathbf{F}}\\ \mathbf{0}\\ \mathbf{0}\\ \mathbf{c}\end{Bmatrix}. \tag{14}$$

Finally, when quasi-static generalized forces and/or displacements are applied, the resulting equation of equilibrium may be condensed in the compact form

$$\begin{bmatrix}\mathbf{K}^*_{\overline{UU}}&\mathbf{K}^*_{\overline{U}\mathbf{\Theta}^\Delta}\\ \mathbf{K}^*_{\mathbf{\Theta}^\Delta\overline{U}}&\mathbf{K}^*_{\mathbf{\Theta}^\Delta\mathbf{\Theta}^\Delta}\end{bmatrix}\begin{Bmatrix}\overline{\mathbf{U}}\\ \mathbf{\Theta}^\Delta\end{Bmatrix}+\begin{Bmatrix}2\overline{\mathbf{F}}\\ \mathbf{c}\end{Bmatrix}=\mathbf{0}, \tag{15}$$

with the nodal average translation $\overline{\mathbf{U}}$ and relative rotation $\mathbf{\Theta}^\Delta$ as independent variables. To obtain these unknowns the equations (15) must be coupled with a limit condition governing the relative rotation and the interaction couples. With the limit condition (2) considered together with the incremental governing equation of the plastic flow, the linear elastoplastic problem is derived

$$\begin{cases}\begin{bmatrix}\mathbf{K}^*_{\overline{UU}}&\mathbf{K}^*_{\overline{U}\mathbf{\Theta}^\Delta}\\ \mathbf{K}^*_{\mathbf{\Theta}^\Delta\overline{U}}&\mathbf{K}^*_{\mathbf{\Theta}^\Delta\mathbf{\Theta}^\Delta}\end{bmatrix}\begin{Bmatrix}\overline{\mathbf{U}}\\ \mathbf{\Theta}^\Delta\end{Bmatrix}+\begin{Bmatrix}2\overline{\mathbf{F}}\\ \mathbf{c}\end{Bmatrix}=\mathbf{0}\\ \varphi_h\left(c_h,\phi_h^\Delta\right)\le 0, h=1,N\\ \delta\phi_h^\Delta=\dfrac{\partial\varphi_h}{\partial c_h}\delta\lambda_h\\ \delta\lambda_h\ge 0,\delta\varphi_h\le 0,\delta\varphi_h\delta\lambda_h=0\end{cases}. \tag{16}$$

Finally the solution of problem (16) may be approached using nonlinear solvers based on Newton-Raphson type schemes in displacement control [69] .

4. Representative problems

Illustrative analytical and numerical experiments are performed to highlight the overall dissipative properties of the proposed layered mechanical metamaterial, where remarkable hysteretic responses are obtained.

4.1. Analytical simulation of a tensioned one-dimensional chain

To highlight the fundamental aspects of the proposed metamaterial, let us consider the one-dimensional stratified chain illustrated in Fig. 4a, consisting of a sequence of opposing disks with radius r, spaced at a distance a and subjected to a tensile force F at the ends. A generic disk is denoted by the index j, with $j-1$ and $j+1$ representing the adjacent disks, respectively. Assuming that the difference in the average displacement $\overline{u}_{j+1}-\overline{u}_j=\overline{u}_j-\overline{u}_{j-1}=\overline{u}$ between contiguous disks is uniform and that the average rotation $\overline{\phi}=0$ and the differential displacement $\mathbf{u}^\Delta=\mathbf{0}$ are zero at all nodes, with the relative rotation between each pair of nodes ϕ^Δ being constant, the first three equations in (12) turn out to be identically satisfied (here, the ligament vectors $\mathbf{n}_i$ and $\mathbf{m}_i$, $i=1,2$, are defined in Fig. 4b). From the fourth equation in (12) the interaction couple is obtained, which depends on the displacement $\overline{\mathbf{u}}$ and the relative rotation ϕ^Δ between adjacent disks in the form

$$c=S_u\overline{u}-S_\phi\phi^\Delta=\frac{Eah}{4}\eta\left(1-\eta^2\right)\sin2\beta\overline{u}-\frac{E\eta a^2h}{4}\left(\sin^2\beta+\eta^2\cos^2\beta\right)\phi^\Delta \tag{17}$$

where the constants S_u and S_ϕ have been defined. The kinematics of the ends of the ligaments of the layers with positive and negative chirality, respectively shown in blue and red in Fig. 4, is illustrated in Fig. 4c. This allows to derive the internal forces in the ligaments and, consequently, the force in the chain, which results as a function of the displacement $\overline{\mathbf{u}}$ and the relative rotation ϕ^Δ in the form

$$F=F_u\overline{u}-F_\phi\phi^\Delta=\frac{2EA}{a\cos\beta}\left(\cos^2\beta+\eta^2\sin^2\beta\right)\overline{u}-\left(1-\eta^2\right)\sin\beta EA\phi^\Delta \tag{18}$$

where the constants F_u and F_ϕ have been defined.

Consider now a virtual tensile test and subsequent unloading of the metasystem, starting from the initial state O, defined as $\overline{u}_o=0$, $\phi_0^\Delta=0$, $c_0=0$. Assume that throughout the loading history the pre-stress in the pins is vanishing, namely $N_0=0$. Consequently, according to (2), state O turns out to be at the limit state $\varphi^*\left(c_0,\phi_0^\Delta,N_0\right)=0$. By applying a monotonically increasing force F to the chain until the relative displacement $\overline{u}_A$ between contiguous disks is reached, it is observed that a relative rotation ϕ^Δ occurs between the contiguous disks. This rotation is accompanied by an increase in the interaction couple, resulting from the dilation resisted by the axial elasticity of the pins. The incremental relationship between the interaction couple and the relative rotation is derived under conditions of remaining in the limit state $\dot{\varphi}^*=0$, resulting in

$$\dot{c}=Y^+\dot{\phi}^\Delta=\frac{k\tan\theta(\tan\theta+f)}{1-f\tan\theta}\dot{\phi}^\Delta \tag{19}$$

where the constant Y^+ is defined. From the finite incremental form of (19) and by substituting into (17), the relative rotation $\phi_A^\Delta=\frac{S_u}{S_\phi+Y^+}\overline{u}_A$ and the interaction couple $c_A=\frac{S_uY^+}{S_\phi+Y^+}\overline{u}_A$ are obtained, respectively, in terms of the displacement at state A. Finally, the tensile force $F_A=\left[F_u-\frac{F_\phi S_u}{S_\phi+Y^+}\right]\overline{u}_A$ is derived, which defines the stiffness of the linear response $O\rightarrow A$, during which frictional dissipation occurs.

Starting from state A, the axial force is reduced, resulting in elastic unloading with no changes in the relative rotation $\dot{\phi}^\Delta=0$. During the unloading phase, the interaction couple is reduced, and the argument of the modulus in the limit state equation (2) changes sign. The elastic unloading ends at state B for which $\varphi^*\left(c_B,\phi_A^\Delta\right)=-c_B+k\tan^2\theta\phi_A^\Delta-f\left[c_B\tan\theta+k\tan\theta\phi_A^\Delta\right]=0$, being $\phi_B^\Delta=\phi_A^\Delta$. The interaction couple $c_B=Y^-\phi_A^\Delta=\frac{k\tan\theta(\tan\theta-f)}{(1+f\tan\theta)}\phi_A^\Delta$ is derived, with $Y^-<Y^+$ when $f>0$. From equation (17) the displacement is obtained $\overline{u}_B=\frac{S_\phi+Y^-}{S_u}\phi_A^\Delta=\frac{S_\phi+Y^-}{S_\phi+Y^+}\overline{u}_A<\overline{u}_A$. The tensile force at state B is then obtained $F_B=\left(F_u-\frac{F_\phi S_u}{S_\phi+Y^-}\right)\overline{u}_B$ together with the stiffness F_u of the elastic unloading. The unloading starting from state B occurs with frictional sliding, with negative values of the argument of the modulus in the limit state equation (2). The incremental relationship between the interaction couple and the relative rotation is derived under conditions of remaining in the limit state $\dot{\varphi}^*=0$, resulting in

$$\dot{c}=Y^-\dot{\phi}^\Delta=\frac{k\tan\theta(\tan\theta-f)}{1+f\tan\theta}\dot{\phi}^\Delta. \tag{20}$$

By combining equations (17) and (18) expressed in incremental form with (2), the incremental relationship between the applied axial force and the average displacement between contiguous cells is obtained

$$\dot{F}=\left(F_u-\frac{F_\phi S_u}{S_\phi+Y^-}\right)\dot{\overline{u}} \tag{21}$$

characterising a linear response in the presence of frictional dissipation, starting from state B and returning all the system variables to the initial state O. The model's response to pulsating axial force is shown in the diagram of Fig. 5, where the dissipative and self-recovering behaviour is illustrated. Interestingly, this behaviour is observed in several dissipative and reusable systems recently proposed in the literature [53,55,57,59,66].

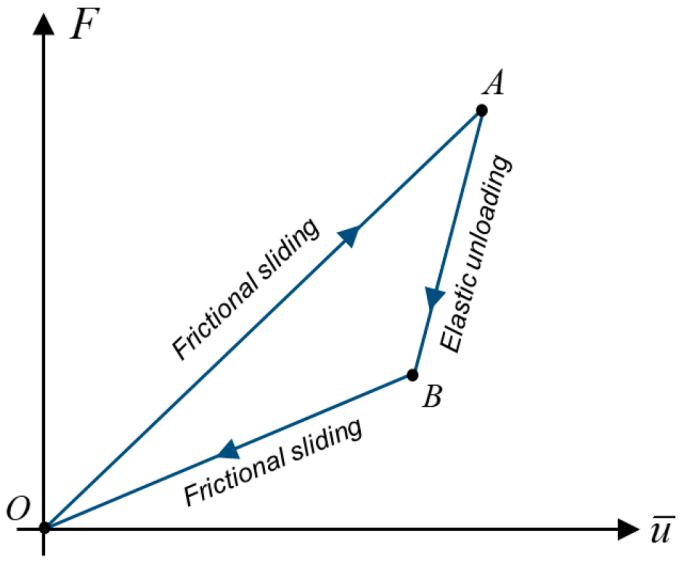

Fig. 5. Tensile loading and unloading of the one-dimensional chain.

4.2. Numerical simulation of the response of dissipative metamaterials

A resilient finite-dimensional meta-device realized with the proposed layered dissipative metamaterials is analysed in detail in this section with the aim of emphasizing the avant-garde performances of the dissipative architecture beam-lattice topologies designed in the paper (see Fig. 1). The discrete Lagrangian formulation detailed in the previous section is implemented in an in-house computer code for linear and non-linear quasi-static simulations.

In Fig. 6 the meta-device is tested in a pseudo-uniaxial strain

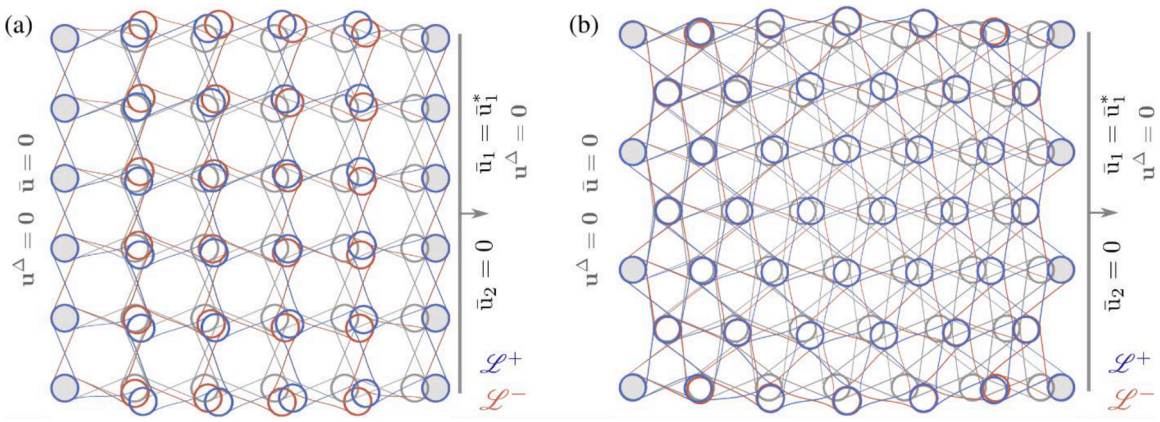

Fig. 6. Detail of the relative displacements between disks of contiguous layers related to pseudo-uniaxial strain conditions: (a) tetrachiral multi-layer systems; (b) hexachiral multi-layer systems. Vanishing pin shear stiffness K_p is assumed for illustrative purposes, with ligaments slenderness ratio $\eta = s/\ell = 1/20$, chirality angle $\beta = \pi/8$, and $\bar{\mathrm{u}}_1^* = a/100$ (grey undeformed configuration, blue deformed configuration and positive chirality, red deformed configuration and negative chirality; displacements magnified by a factor $M = 30$).

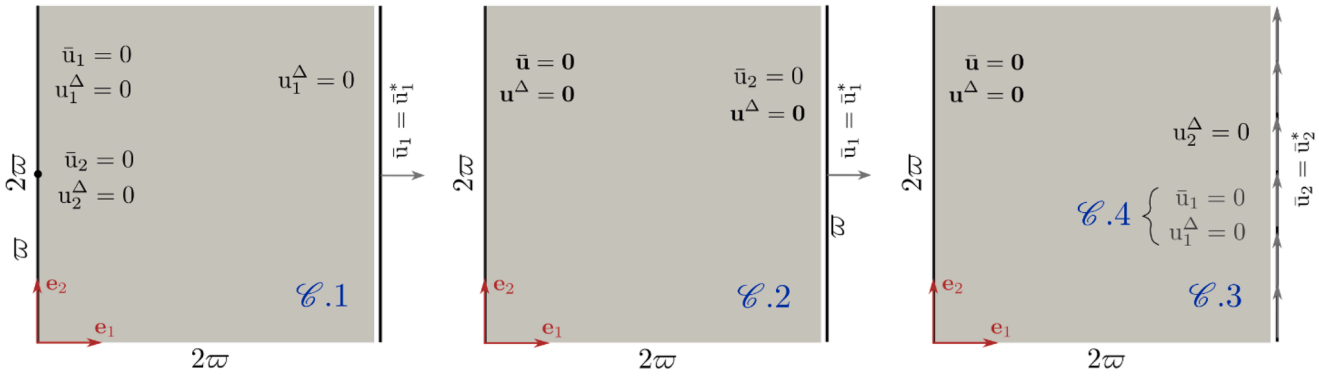

Fig. 7. Layout of the four mechanical tests: $\mathscr{C}.1$, $\mathscr{C}.2$ (extension) and $\mathscr{C}.3$, $\mathscr{C}.4$ (shear-bending) performed on chiral honeycombs multi-layer systems with opposite chirality. The specimen size is $L = 2\varpi = na$.

condition (with free rotation of the disks of the layers) for the tetrachiral and hexachiral topologies for the limit case of vanishing pin shear stiffness. It is noted that there are fundamental differences in the elastic behaviour among the different topologies under study. It is important to emphasize that for the hexachiral topology, sufficiently far from the edges (i.e., in regions with fully linked, rigid circles), the relative displacements between adjacent layers of opposing chirality appear to be evanescent, even in the limiting case of vanishing pin shear stiffness. This evidence has already been demonstrated in the case of arbitrary affine displacement fields for a generic shear stiffness of the pins in Bacigalupo *et al.* [65] and is mainly due to the effective elastic isotropy of the system. On the contrary, in the case of tetrachiral topology, relative displacements are observed whose magnitude depends, with other conditions being equal, on the shear stiffness of the pins in the assumptions of free rotations of the disks of the layers. This behaviour is due to the anisotropy of the tetrachiral system and is proved in [70].

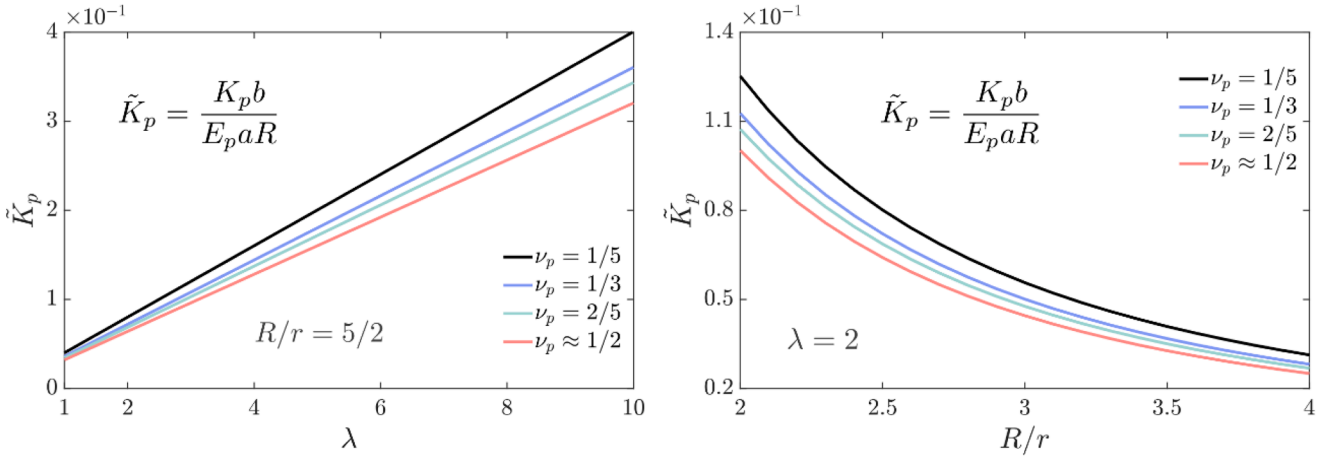

Fig. 8. Analytical dependence of the pin shear stiffness in terms of the mechanical parameters: (left) $\tilde{K}_p$ v.s. λ; (right) $\tilde{K}_p$ v.s. nondimensional ratio R/r.

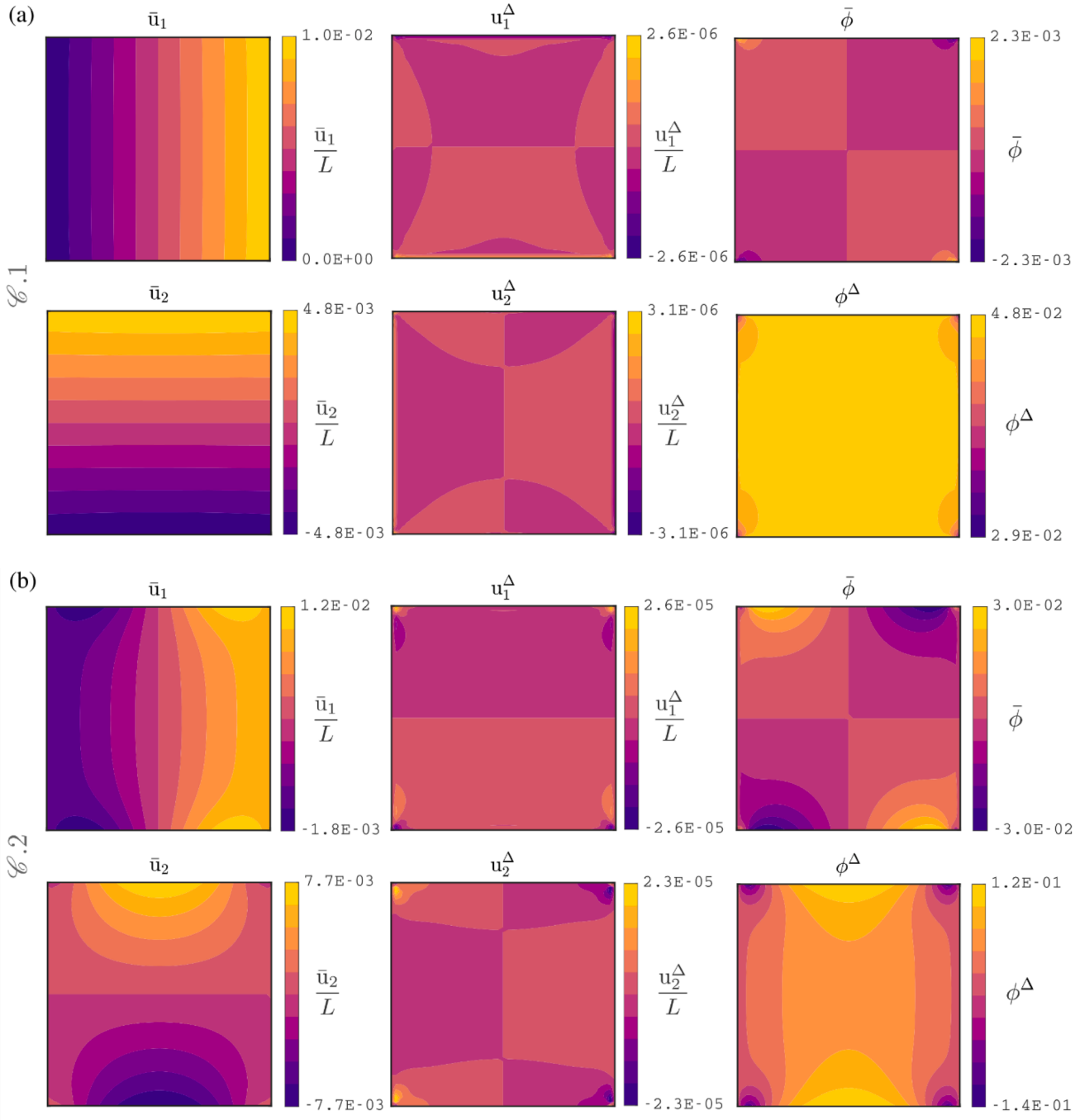

Fig. 9. Elastic mechanical tests on multi-layer systems with free relative rotations. Displacement and rotation fields corresponding to the mechanical tests $\mathscr{C}.1$ (a) and $\mathscr{C}.2$ (b) performed on tetrachiral honeycombs multi-layer system ($L = 2\varpi = na$ with $n = 50$). The imposed displacement is $\overline{u}_1^* = L/100$, while $\beta = \pi/8$. The pins shear stiffness K_p is obtained assuming $b = 9a/40$.

The hexa-tetrachiral topology, however, manifests fully anisotropic global elastic properties in a single layer (see Bacigalupo *et al.* [70] for details) and, as will be shown later, exhibits overall characteristics that are intermediate between those of the other two topologies. Therefore, based on the preceding discussion and to isolate the chiral properties resulting from the SO(2) invariance of the hemitropic part of the global elastic tensor of the monolayer (which leads to equivalent bulk strain-rotation coupling [71,72]), this section focuses on tetrachiral and hexachiral stratified systems. Specific attention is given to the tetrachiral topology due to the presence, in general, of relative displacements between the non-vanishing layers.

To highlight the overall elastic and dissipative properties of the designed meta-devices four mechanical tests are performed. The layout of the numerical experiments considered is depicted in Fig. 7. Specifically, the mechanical tests $\mathscr{C}.1$ and $\mathscr{C}.2$ involve imposed axial displacement (with the first characterized by conditions of pseudo-homogeneity of equivalent deformations), whereas the $\mathscr{C}.3$ and $\mathscr{C}.4$ tests involve imposed transversal displacement of bending-like and simple shear-like types, respectively.

The pin shear stiffness K_p can be obtained by assuming, for simplicity, simple shear conditions among contiguous periodic layers with respect to relative displacements. Hence, we may define

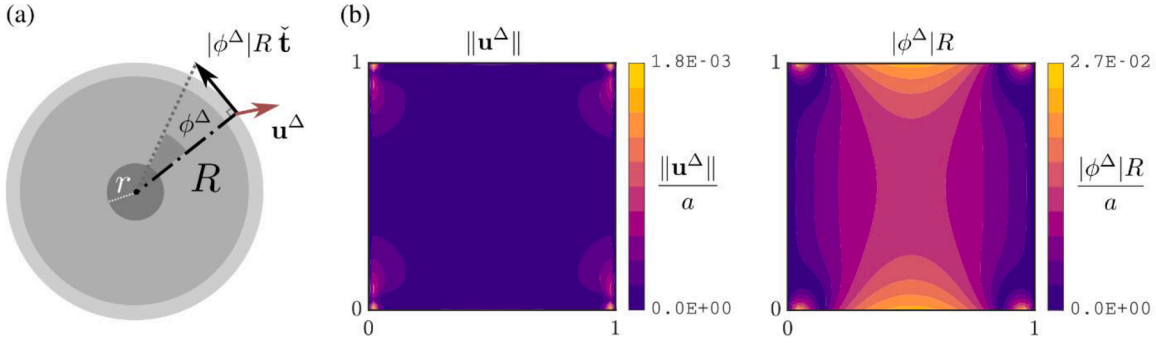

Fig. 10. Relative displacements and relative rotations. Schematics of the relative displacement vector $\mathbf{u}^{\Delta}$ and disks edge displacement $|\phi^{\Delta}|R$**tildet** caused by the relative rotation of two contiguous disks; (a) and detail of the two nondimensional displacement maps corresponding to the elastic test $\mathscr{E}.2$ with $\overline{u}_1^* = L/100$, $\beta = \pi/8$ and $b = 9a/40$ ($L = 2\varpi = na$ with $n = 50$). The unit vector in the generic direction normal to the disk radius is denoted by **tildet**.

$$K_p = \frac{\lambda \pi r^2 G_p}{b}, \tag{22}$$

where λ is the nondimensional parameter determining the height of the deformed pin portion, and G_p is the shear modulus of the constituent homogeneous, isotropic material. The dependence of the nondimensional pin shear stiffness $\widetilde{K}_p = K_p b/(E_p a R)$ on the nondimensional parameters λ and r/R, considering different materials, is shown in Fig. 8.

If not otherwise specified, the adopted slenderness ratio of the ligaments is $\eta = s/\ell = 1/20$, the inner radius of the disks is $r = 2R/5$, the nondimensional ratio $\lambda = 2$, while pins are assumed to be made of TEEKAPEEK natural, a polymeric material characterized by Young modulus $E_p = 4.2$GPa and Poisson ratio $\nu_p = 0.37$ (in agreement of the materials used in Bacigalupo *et al.* [66]). Disks and ligaments are here assumed made of stainless steel with Young modulus being $E = 195$GPa. In the case of frictional-dilatant interfaces, if not otherwise specified, the thickness nondimensional ratio is $h/b = 3/4$, the inclination angle of the teeth is $\theta = \pi/6$, whereas the friction coefficient is $f_r = 0.75$ (stainless steel-stainless steel). These representative parameters are the result of a preliminary optimization study of the elastic and dissipative properties of the mechanical metamaterial [66]; however, their specific values do not alter the qualitative and general character of the results shown in this section.

Fig. 9 shows the typical displacement and rotation fields corresponding to the elastic axial mechanical tests $\mathscr{E}.1$ and $\mathscr{E}.2$ performed on tetrachiral multi-layer systems with free relative rotations. It is important to note that the relative displacements are greatly influenced not only by the stiffness of the pins but also by the dimensions of the microstructure in relation to the global dimensions of the specimen. They appear to be generally negligible when $L/a = n \geq 50$. It is assumed that relative displacements affect, at most, only the elastic response of the system. Given that these (relative) displacements are generally at least an order of magnitude smaller than the disks edge displacements caused by the relative rotation of two contiguous disks, their influence on the dissipative properties of the interfaces is considered negligible (see Fig. 10).

Considering multi-layer (tetrachiral) systems with frictional non-dilatant rigid-plastic interfaces, i.e. $\theta = 0$, the results of the elastic-plastic analyses obtained under cyclic displacement control highlight important general behavioral evidence, as shown in Fig. 11 for different specimen sizes, with the aim of appreciating size-effect. It is noted that the global dissipative properties corresponding to tests $\mathscr{E}.1$ and $\mathscr{E}.2$ are significantly greater than those of the other two tests. This evidence is motivated by the fact that the first two tests exhibit axial-dominated deformation, while the other two are dominated by bending and shear (the last outcome agrees with the homogenous model analyzed in Bacigalupo et al. 2023). The dissipative properties of the system are due to the rotation field defined at the level of a single layer, which, in chiral systems of this kind, is elastically coupled to axial (bulk) deformation. Therefore, in tests $\mathscr{E}.3$ and $\mathscr{E}.4$, the deformation appears to be highly non-homogeneous and bending-shear dominated, with shear deformation that, by definition, does not imply relative rotation between the layers and consequently does not generate dissipation (see Fig. 11). Consequently, it is important to underline that the size effect of the elastic response is more pronunciated as the global non-homogeneity of the deformation increases (see Figs. 11b,c). In any case, it is noted that the behavior of the cyclic response of the multilayer metamaterial turns out to be size independent in the case $L/a = n \geq 25$.

The pseudo-affine displacement field associated with the $\mathscr{E}.1$ test allows for a comparison between the obtained results and the analytical solution corresponding to a homogeneous generalized micropolar continuum equivalent to the multilayered lattice-like material (Bacigalupo *et al.* [66,70]). In this case, very good agreement is observed between the numerical and analytical predictions (Fig. 11c). For the above reasons, the following discussion focuses on mechanical tests with axially dominated deformation. Another consideration is that, in correspondence with the plasticized sub-domains (e.g. where relative rotations are free), the metamaterial exhibits a globally auxetic behavior (Fig. 11c).

Regarding the case of frictional dilatant self-recovering interfaces, Fig. 12 shows that the resulting deformation is self-recovering at the end of the equivalent load cycle, theoretically rendering the mechanical metamaterial infinitely reusable or resilient, accordingly with the simple illustrative one-dimensional model analysed in Section 4.1. In the specific case of test $\mathscr{E}.1$, the aforementioned conditions of pseudo-homogeneity combined with the hypothesis of vanishing initial pin traction $N_0 = 0$, imply a negligible size effect on the global cyclic response (Fig. 12a,c), with the plastic regime almost instantaneously achieved throughout the domain in both the loading and unloading phases. In this case as well, the results obtained are consistent with analytical predictions corresponding to an equivalent micropolar continuum (see [65]) It is important to note that the dissipative properties of the material depend on the chirality angle. Specifically, within the range of values studied, dissipation tends to increase as the chirality angle increases (see Fig. 12a). In particular, the chirality angle β has a greater impact on the system's overall stiffness during the unloading stage compared to the loading stage.

It is worth underlining that the same behaviour observed under tensile loads may be obtained under compression (see [65]). Fig. 13 shows the dissipative properties of the material corresponding to a full tensile-compressive cycle while assuming different values of the friction coefficient f. It is noted that, in this case, the friction coefficient plays an important role on the cyclic dissipation as well as in modifying the overall stiffness of the system during the loading stage rather than the unloading stage (Fig. 13).

While the specific value of the nondimensional ratio $\delta = h/b$, for a given thickness b, friction coefficient, and angle θ, does not substantially alter the overall response of the system, it is observed that, as expected,

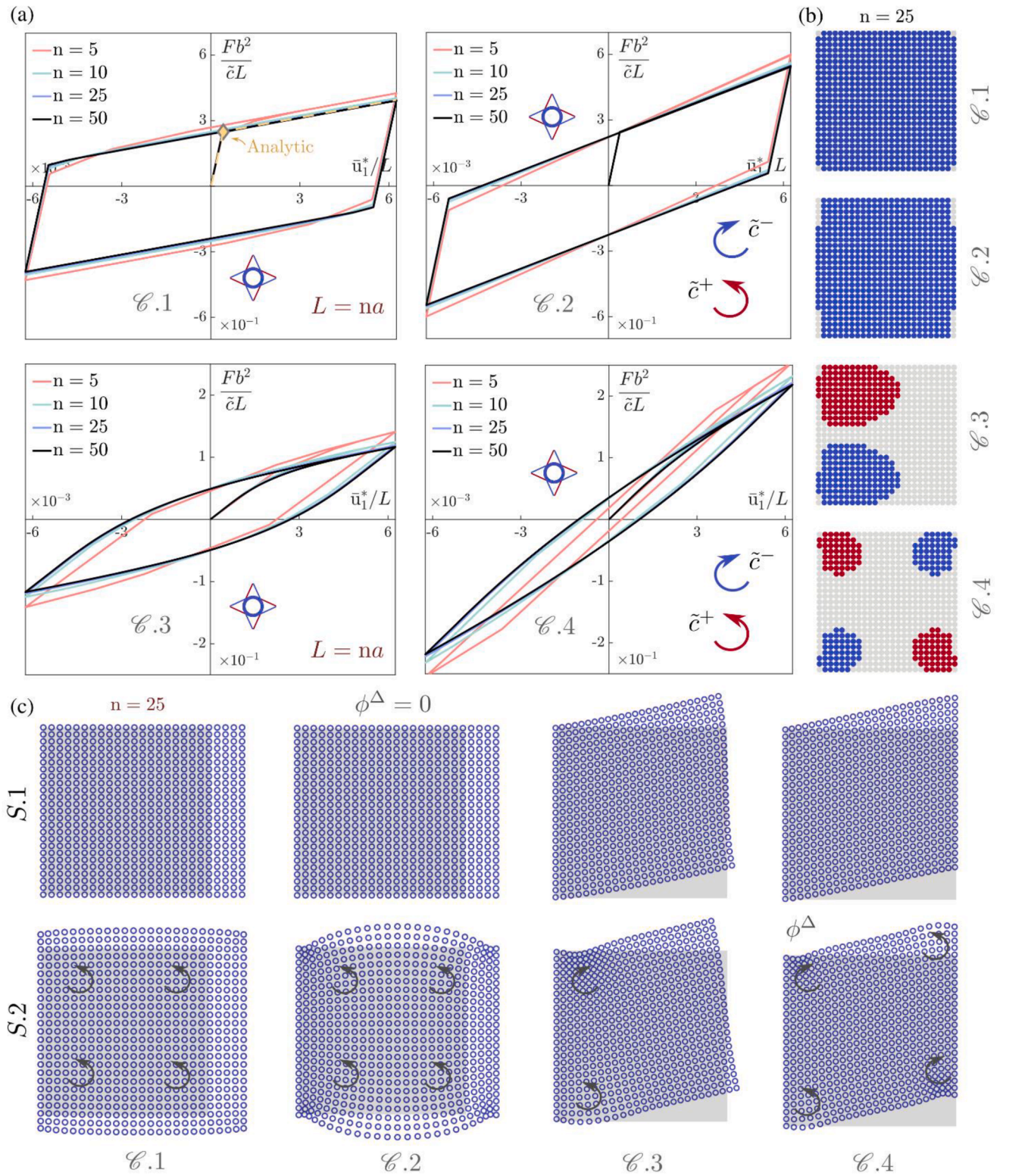

Fig. 11. Multi-layer (tetrachiral) system with frictional non-dilatant rigid-plastic interfaces. (a) Normalized force-displacement curves corresponding to a full load cycle and referred to the four mechanical tests, performed considering different specimen size while assuming $b = h = 9a/40$, $\beta = \pi/8$; (b) Map of the plastic zones (e.g. rings interfaces satisfying the limit condition) corresponding to the maximum imposed displacement $\bar{u}_i^* = \hat{\bar{u}}_i^* = L/160$ in the four mechanical tests. Red and blue colours denote positive and negative sign of the interface couple at the frictional limit state $\tilde{c}$, respectively; (c) Deformed configurations corresponding to $\bar{u}_i^* = \hat{\bar{u}}_i^*/100$ (elastic regime, stage *S*.1) and $\bar{u}_i^* = \hat{\bar{u}}_i^*$ (plastic regime, stage *S*.2). Displacements are magnified by a factor $M = 3 \times 10$ (*S*.1) and $M = 3 \times 10^3$ (*S*.2) for better visualization. In the case of $\mathscr{C}.1$ and $\mathscr{C}.2$ tests, F denotes the horizontal reaction force, whereas in the case of $\mathscr{C}.3$ and $\mathscr{C}.4$ tests, it denotes the vertical reaction force.

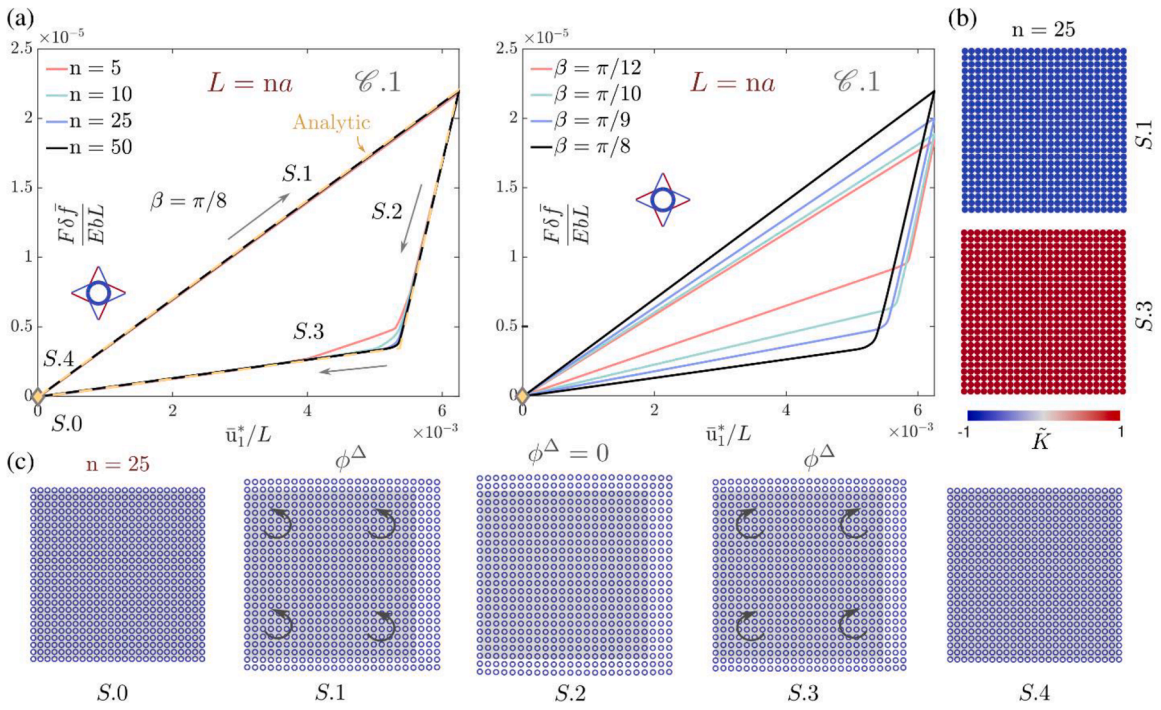

Fig. 12. Multi-layer (tetrachiral) system with frictional dilatant self-recovering interfaces. (a, left) Normalized force-displacement curves referred to the mechanical test $\mathscr{C}.1$ and corresponding to different specimen sizes while assuming $\beta = \pi/8$ and $b/a = 3/10$; (a, right) Influence of the chirality angle on the overall dissipative properties of the tetrachiral system in the case of a sufficiently large specimen with $n = 25$; (b) Map of the plastic zones (e.g. rings interfaces satisfying the limit condition) corresponding to $\bar{u}_i^* = L/250$ (plastic regime-*loading*, step *S*.1 and plastic regime-*unloading*, step *S*.3) with $\widetilde{K} = \hat{c}/|\hat{c}|$ being the actual normalized interface resistance couple; (c) Deformed configurations obtained with $n = 25$, $\beta = \pi/8$ and corresponding to $\bar{u}_i^* = L/250$ (plastic regime-*loading*, step *S*.1 and plastic regime-*unloading*, step *S*.3) and $\bar{u}_i^* = L/175$ (elastic return, step *S*.2). The initial and final stages are referred to as *S*.0 and *S*.4, respectively.

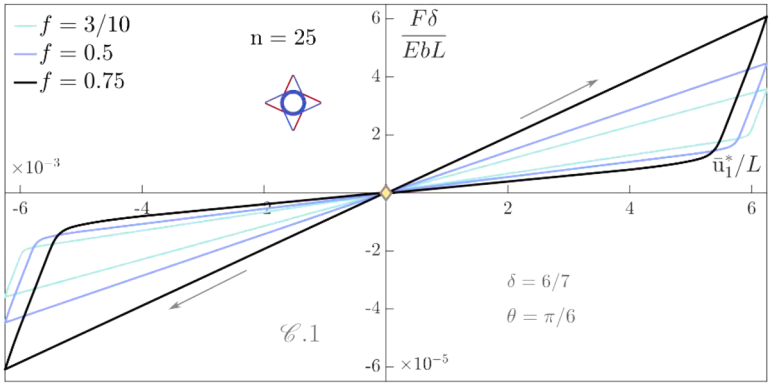

Fig. 13. Multi-layer (tetrachiral) system with frictional dilatant self-recovering interfaces. Normalized force-displacement curves referred to the mechanical test $\mathscr{C}.1$ with $b/a = 3/10$ and $\delta = 6/7$, corresponding to a full tensile-compressive cycle, while assuming different values of the friction coefficient f.

the specific value of the angle — when the other parameters are fixed — can significantly modify the overall stiffness of the system, predominantly in the loading stage (Fig. 14). This behaviour is similar to that previously observed and is related to the variation of the friction coefficient f.

The recentering properties are also verified in the case of non-homogeneous deformation (in reference to the test $\mathscr{C}.2$), while size-independent behaviour occurs, as in the case of non-dilating interfaces when $L/a = n \geq 25$. It is also noted that the conditions of non-homogeneity characterizing the $\mathscr{C}.2$ test, although substantially modifying the response and cyclical trend of the mechanical system, do not substantially influence the resulting dissipative properties of the system, both in the case of dilating and non-dilating interfaces (see Fig. 15). As observed previously, the extent of relative displacements between the layers is affected by scale effects of the microtructure as well as, under equal conditions, by the stiffness of the pin. It is interesting to observe that for evanescent K_p, the $\mathscr{C}.2$ test tends towards that corresponding to the conditions of pseudo-homogeneity typical of the $\mathscr{C}.1$ test (Fig. 15). Furthermore, it is important to underline that, unlike the case of non-dilating interfaces, dissipation tends to increase as the chirality angle decreases (see Fig. 15b).

Finally, the diagrams in Fig. 16 show an effective stiffness of the tetra-hexachiral metamaterial, in the tested direction, is, in general, larger than that of the tetrachiral metamaterial, while the resulting dissipative properties are remarkable. This behavior appears to be in good agreement with the results in Bacigalupo *et al.* [66,70]. It is confirmed that the pin shear stiffness does not influence the global response of the hexachiral system under the loading and unloading

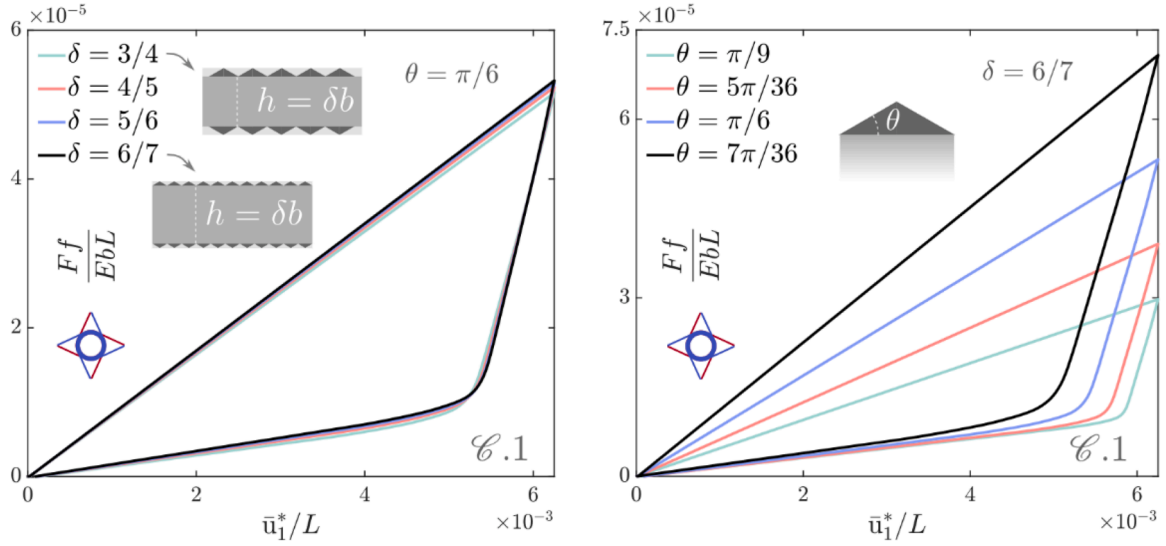

Fig. 14. Multi-layer (tetrachiral) system with frictional dilatant self-recovering interfaces. Normalized force-displacement curves referred to the mechanical test $\mathscr{C}.1$ with $b/a = 3/10$, corresponding to different values of the nondimensional ratio $\delta = h/b$ (left) and different angles θ (right).

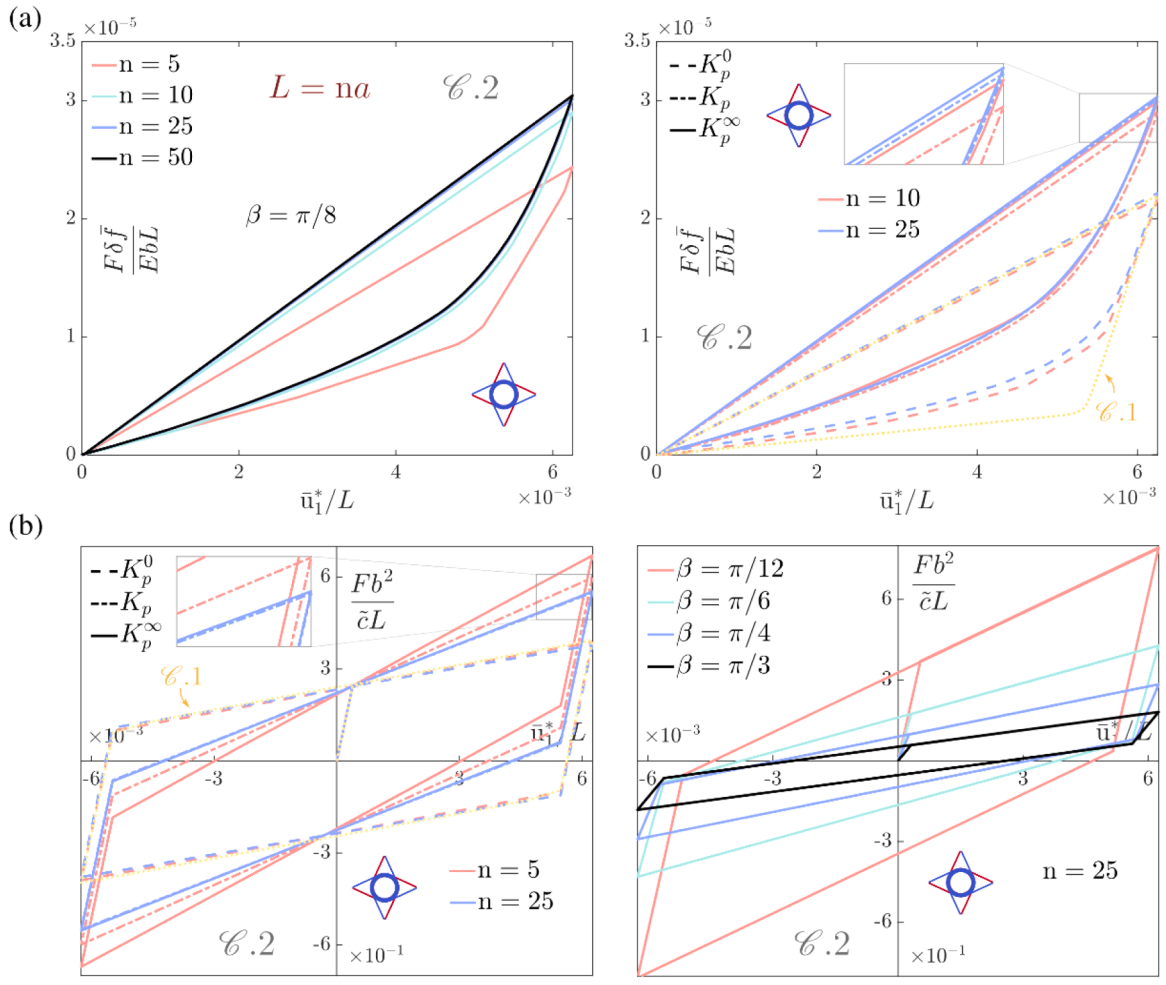

Fig. 15. Multi-layer (tetrachiral) system with frictional dilatant self-recovering interfaces. (a, left) Normalized force-displacement curves referred to the mechanical test $\mathscr{C}.2$ with $b/a = 3/10$ and $\beta = \pi/8$, corresponding to different specimen size; (a, right) Influence of the pin shear stiffness and specimen size on the overall dissipative response of the layered material; (b, left) Multi-layer (tetrachiral) system with frictional non-dilatant rigid-plastic interfaces (mechanical test $\mathscr{C}.2$ with $b = h = 9a/40$): Influence of the pin shear stiffness and specimen size on the overall dissipative response of the layered material; (b, right) Influence of the chirality angle on the overall dissipative properties of layered material in the case of a sufficiently large specimen with $n = 25$.

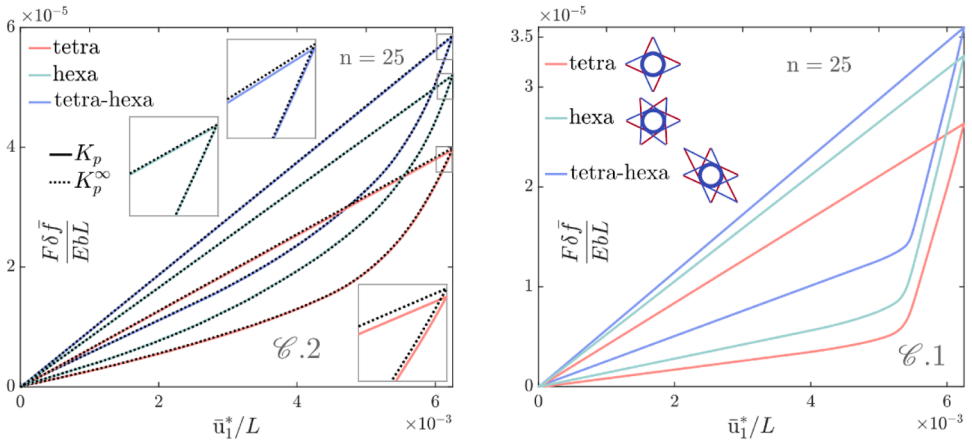

Fig. 16. Multi-layer systems with frictional dilatant self-recovering interfaces. (left) Normalized force-displacement curves referred to the mechanical test $\mathscr{C}.2$ (with $n = 25$, $b/a = 3/10$, $\delta = 6/7$ and $\beta = \pi/8$), obtained considering tetrachiral, hexachiral and tetra-hexachiral topologies and corresponding to different pin shear stiffness; (right) Influence of lattice topology, i.e. tetrachiral, hexachiral and tetra-hexachiral, on the overall stiffness and dissipative properties of the layered material in the case of sufficiently large specimens and corresponding to the mechanical test $\mathscr{C}.1$ (with $n = 25$, $b/a = 3/10$, $\delta = 6/7$ and $\beta = \pi/8$).

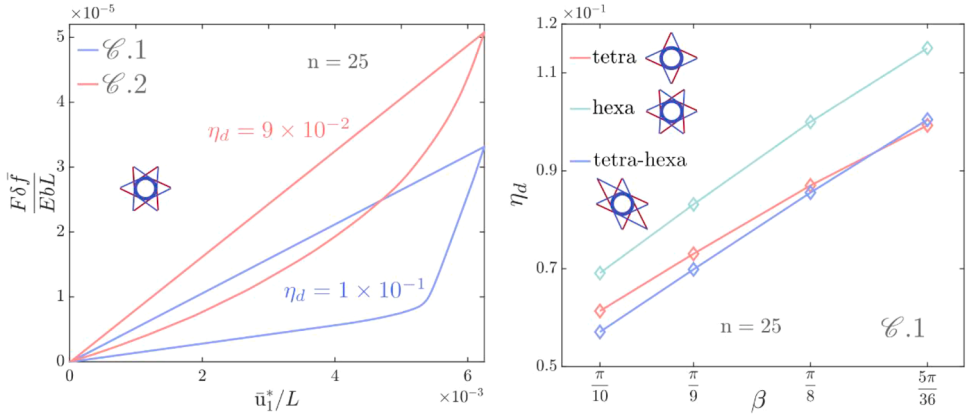

Fig. 17. Multi-layer systems with frictional dilatant self-recovering interfaces. (left) Normalized force-displacement curves corresponding to the mechanical tests $\mathscr{C}.1$ and $\mathscr{C}.2$ ($n = 25$, $b/a = 3/10$, $\delta = 6/7$), obtained considering $\beta = \pi/8$ and the hexachiral topology, with indication of the loss coefficient obtained η_d; (right) Loss coefficient η_d corresponding to the hexachiral, tetrachiral and tetra-hexachiral topologies as function of the chirality angle (mechanical test $\mathscr{C}.1$).

stages, while it turns out to modify the stiffness of the system in the case of tetrachiral topology. The tetra-hexachiral microstructure shows intermediate properties among those mentioned above (Fig. 16). According to the plastic-attritive admissibility condition (2), dissipation properties appear to depend on the thickness of a single layer through the specific value of the geometric parameter b, as greater thicknesses are associated, in general, with lower dissipative characteristics. This property holds for all the microstructure topologies considered. Another noteworthy point is that the tetra-hexachiral system exhibits overall behavior, in the tested direction, similar to that of the other microstructures, with effective elastic stiffness aligning more closely with that of the hexachiral system than the tetrachiral system, while the dissipative properties, within the studied conditions, turn out to be closer to those characterizing the tetrachiral topology (see Fig. 17).

In any case, considering the tested directions and the range of parameters studied, the hexachiral topology appears to be associated with the highest dissipation compared to the other microstructures (Fig. 17). The dissipation properties are estimated by the loss coefficient η_d, i.e. the equivalent damping ratio of the hysteretic model (see Ashby [73] and Bacigalupo *et al.* [66] for details). The hexachiral topology theoretically offers elastic and dissipative isotropic properties, whereas the tetrachiral and tetra-hexachiral microstructures are characterized by direction-dependent properties owing to different material symmetries. However, tetrachiral and tetra-hexachiral topologies allow for the preparation of regular square grids, which simplifies the testing conditions of the periodic specimens. Hence, the selection between different microstructures may hinge upon specific technological requirements, such as the ability to establish reliable gripping/loading systems, the nature of the forces under consideration, and, crucially, the resistance properties of the materials adopted. The maximum loss coefficient obtained in this paper (see Fig. 17), which is consistent with the value obtained analytically for a micropolar continuum equivalent to the stratified lattice in Bacigalupo et al. [65], is reported in the Ashby chart [73] in Fig. 18. This result demonstrates how it is possible to achieve both high dissipation and stiffness, one of the desired properties in this study.

5. Conclusions

A novel design strategy is introduced for developing resilient, high-energy-dissipating metamaterials tailored for reusable and self-restoring mechanical metadevices. This approach integrates stretchable, self-tensioning elastic components with frictional-dilating mechanisms, where energy dissipation occurs through controlled inelastic micro-deformations. A stratified metamaterial design is proposed, consisting of chiral beam-lattice structures formed by rigid disks connected with elastic ligaments and stacked using elastic pins. The alternating chirality of the lattices induces relative rotations between adjacent disks

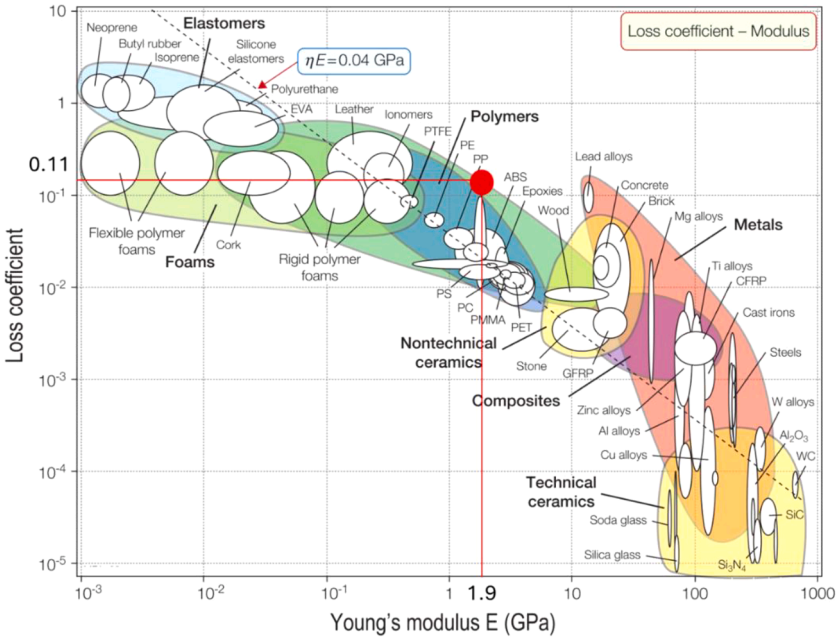

Fig. 18. Performance of the designed resilient metamaterial: the loss coefficient of the hexachiral stratified metamaterial plotted against Young's modulus (red circle) in the Ashby chart [73].

in opposing layers, which are regulated by frictional contact. This innovative configuration harnesses the interaction between elastic deformation and frictional forces, enabling a precisely controlled energy dissipation mechanism. The frictional disk-to-disk interface can be either flat or jagged. In the first case, the material model exhibits linear hardening plastic behavior, while in the latter, the imposed dilation interacts with the axial elasticity of the pins, resulting in a self-recovering response. The meta-device is described using a discrete Lagrangian model and the response to various pulsating and cyclic load histories is obtained. Numerical tests have been conducted on simple square specimens to vary the disk density (i.e., the number of disks per unit area) and boundary conditions. These tests are designed to capture both homogeneous and inhomogeneous deformation modes under overall traction and bending conditions. For flat disk-to-disk interfaces, the response to overall traction is found to be bilinear elastic-plastic, with only a slight dependence on cell density. Additionally, a sensitivity to disk density is observed in the bending tests, where the response is characteristic of a system undergoing progressive plasticization. For frictional dilatant disk-to-disk interfaces, the uniaxial response under homogeneous boundary conditions exhibits a trilinear behavior, characterized by high energy dissipation and a self-recovering response. This particular response is explained in the paper by considering the uniaxial response of a simple one-dimensional model. Moreover, from the numerical examples it turns out that the chirality of the lattice and the asperity angle of the interface play a significant role in influencing the energy dissipation. In case of non-homogeneous boundary conditions, the overall qualitative response remains largely unchanged. However, for both frictional interfaces considered, the disk density per unit area has an impact on the hysteretic response and on the energy dissipated. Further analyses have focused on comparing the dissipative capacity of tetrachiral, hexachiral and tetra-hexachiral lattices in the case of frictional-dilatant interfaces. Since the metamaterial exhibits the same response to global uniaxial tensile and compressive forces, the cyclic tension-compression response was considered, allowing for the evaluation of the loss coefficient, which measures the energy dissipated in a cycle relative to the elastic energy stored and turns out to be increasing with the chirality angle. Based on the comparisons conducted, it appears that the hexachiral topology demonstrates the highest loss coefficient. By considering realistic geometric and material parameters, it was observed that the hexachiral metamaterial achieves a higher loss coefficient and greater stiffness compared to other dissipative lattice topologies.

In conclusion, while experimental validation is still needed, the proposed metamaterial appears to offer the following advantages over existing technologies: i) a hysteretic response with high mechanical dissipation and stiffness; ii) the ability to reuse the device without external intervention, restoring its initial configuration after deformation; iii) a multi-directional dissipative response; and iv) a bilateral response, ensuring consistent performance under both tension and compression.

CRediT authorship contribution statement

Andrea Bacigalupo: Writing – review & editing, Writing – original draft, Validation, Software, Methodology, Investigation, Formal analysis, Conceptualization. **Vito Diana:** Writing – review & editing, Writing – original draft, Validation, Software, Methodology, Investigation, Formal analysis, Conceptualization. **Luigi Gambarotta:** Writing – review & editing, Writing – original draft, Validation, Software, Methodology, Investigation, Formal analysis, Conceptualization.

Declaration of competing interest

The authors declare that they have no known competing financial interests or personal relationships that could have appeared to influence the work reported in this paper.

Acknowledgments

A.Bacigalupo is member of INdAM-GNFM. The authors gratefully acknowledge the National Group of Mathematical Physics (GNFM-INdAM, Italy) and the financial support of the European Union - Next Generation EU, component M4C2, investment 1.1 for the project PRIN PNRR 2022-P2022HLHHB-D53D23018260001: "A digital framework for the cutting of soft tissues: A first step towards virtual surgery".

Data availability

No data was used for the research described in the article.

References

[1] Corsaro RD, Sperling LH. Sound and Vibration Damping with Polymer. American Chemical Society Press; 1990.
[2] Lu G, Yu TX. Energy absorption of structures and materials. Elsevier; 2003.
[3] Sperling LH. Introduction to Physical Polymer Science. Wiley; 2006.
[4] Gibson LJ, Ashby MF. Cellular Solids: Structure and Properties. Cambridge, UK: Cambridge University Press; 1997.
[5] Guell Izard A, Bauer J, Crook C, Turlo V, Valdevit L. Ultrahigh energy absorption multifunctional spinoidal nanoarchitectures. Small 2019;15:1903834.
[6] Unwin AP, Hine PJ, Ward IM, Fujita M, Tanaka E, Gusev AA. Escaping the Ashby limit for mechanical damping/stiffness trade-off using a constrained high internal friction interfacial layer. Sci Rep 2018;8:2454.
[7] Zhang J, Lu G, You Z. Large deformation and energy absorption of additively manufactured auxetic materials and structures: a review. Compos Part B: Eng 2020; 201:108340.
[8] Ma J, Chai S, Chen Y. Geometric design, deformation mode, and energy absorption of patterned thin-walled structures. Mech Mater 2022;168:104269. c.
[9] Bohara RP, Linforth S, Nguyen T, Ghazlan A, Ngo T. Anti-blast and-impact performances of auxetic structures: a review of structures, materials, methods, and fabrications. Eng Struct 2023;276:115377.
[10] Hu Q, Zhang X, Zhang J, Lu G, Tse KM. A review on energy absorption performance of auxetic composites with fillings. Thin-Walled Struct 2024:112348.
[11] Zhang J, Lu G, Ruan D, Wang Z. Tensile behavior of an auxetic structure: analytical modeling and finite element analysis. Int J Mech Sci 2018;136:143–54.
[12] Schaedler TA, Ro CJ, Sorensen AE, Eckel Z, Yang SS, Carter WB, Jacobsen AJ. Designing metallic microlattices for energy absorber applications. Adv Eng Mater 2014;16:276–83.
[13] Tancogne-Dejean T, Spierings AB, Mohr D. Additively-manufactured metallic micro-lattice materials for high specific energy absorption under static and dynamic loading. Acta Mater 2016;116:14–28.
[14] Wang P, Yang F, Ru D, Zheng B, Fan H. Addittive-manifactured hierarchical multi-circular lattice structures for energy absorption application. Mater Des 2021;210: 110116.
[15] Xiao L, Xu X, Feng G, Li S, Song W, Jiang Z. Compressive performances and energy absorption of additively manufactured metallic hybrid lattice structures. Int J Mech Sci 2022;219:107093.
[16] Liang H, Sun B, Hao W, Sun H, Pu Y, Ma F. Crashworthiness of lantern-like lattice structures with a bidirectional gradient distribution. Int J Mech Sci 2022;236: 107746.
[17] Meza LR, Das S, Greer JR. Strong, lightweight, and recoverable three-dimensional ceramic nanolattices. Science (1979) 2014;345(6202):1322–6.
[18] Meza LR, Zelhofer AJ, Clarke N, Mateos AJ, Kochmann DM, Greer JR. Resilient 3D hierarchical architected metamaterials. *Proc Nat Acad Sci* 2015;112:11502–7.
[19] Vuyk P, Harne RL. Collapse characterization and shock mitigation by elastomeric metastructures. Extr Mech Letts 2020;37:100682.
[20] Zhang D, Li M, Qiu N, Yang J, Wu C, Steven G, Fang J. 4D-printed reusable metamaterial via shape memory effect for energy dissipation. Int J Mech Sci 2024; 275:109309.
[21] Shan S, Kang SH, Raney JR, Wang P, Fang L, Candido F, Lewis JA, Bertoldi K. Multistable architected materials for trapping elastic strain energy. Adv Mater 2015;27:4296–301.
[22] Restrepo D, Mankame ND, Zavattieri PD. Phase transforming cellular materials. Extr Mech Lett 2015;4:52–60.
[23] Frenzel T, Findeisen C, Kadic M, Gumbsch P, Wegener M. Tailored buckling microlattices as reusable light-weight shock absorbers. Adv Mater 2016;28: 5865–70.
[24] Findeisen C, Hohe J, Kadic M, Gumbsch P. Characteristics of mechanical metamaterials based on buckling elements. J Mech Phys Sol 2017;102:151–64.
[25] Kidambl N, Harne RL, Wang KW. Energy capture and storage in asymmetrically multistable modular structures inspired by skeletal muscle. Smart Mat Struct 2017; 26:085022.
[26] Ha CS, Lakes RS, Plesha ME. Design, fabrication and analysis of lattice exhibiting energy absorption via snap-through behavior. Mater Des 2018;141:426–37.
[27] Zhang Y, Restrepo D, Velay-Lizancos M, Mankame ND, Zavattieri PD. Energy dissipation in functionally two-dimensional phase transforming cellular materials. Sci Rep 2019;9:12581.
[28] Yan S, Wu L, Meng Z, Tan X, Liu W, Wen Y, Zhou J. Double-strip metamaterial for vibration isolation and shock attenuation. Int J Mech Sci 2024;282:109686.
[29] Rossi N, Méndez CG, Huespe AE. Surrogate model for a mechanical metamaterial undergoing microstructure instabilities and phase transformations. Int J Mech Sci 2023;243:107913.
[30] Rossi N, Romero I, Huespe AE. On the limit behavior of lattice-type metamaterials with bi-stable mechanisms. Int J Mech Sci 2024;276:109375.
[31] Chen YL, Ma L. A minimalist elastic metamaterial with meta-damping mechanism. Int J Solids Struct 2024;302:112977.
[32] Liu S, Azad AI, Burgueno R. Architected materials for tailorable shear behavior with energy dissipation. Extr Mech Lett 2019;28:1–7.
[33] Tan X, Wang B, Yao K, Zhu S, Chen S, Xu P, Sun Y. Novel multi-stable mechanical metamaterials for trapping energy through shear deformation. Int J Mech Sci 2019; 164:105168.
[34] Tan X, Wang B, Zhu S, Chen S, Yao L, Xu P, WU L, Sun Y. Novel multidirectional negative stiffness mechanical metamaterials. Smart Mater Struct 2020;29:015037.
[35] Benichou I, Givli S. Force-sensitive metamaterials for vibration mitigation and mechanical protection. Extr Mech Lett 2020;40:100932.
[36] Tan X, Chen S, Zhu S, Wang B, Xu P, Yao K, Sun Y. Reusable metamaterial via inelastic instability for energy absorption. Int J Mech Sci 2019;155:509–17.
[37] Li Q, Yang D, Ren C, Mao X. A systematic group of multidirectional buckling-based negative stiffness metamaterials. Int J Mech Sci 2022;232:107611.
[38] Ma H, Wang K, Zhao H, Mu R, Yan B. A reusable metastructure for tri-directional energy dissipation. Int J Mech Sci 2022;214:106870.
[39] Ma H, Wang K, Zhao H, Shi W, Xue J, Zhou Y, Yan B. Energy dissipation and shock isolation using novel metamaterials. Int J Mech Sci 2022;228:107464.
[40] Liang H, Sun B, Hao W, Sun H, Pu Y, Ma F. Crashworthiness of lantern-like lattice structures with a bidirectional gradient distribution. Int J Mech Sci 2022;236: 107746.
[41] Hector KW, Restrepo D, Tejedor Bonilla C, Hector L, Mankame N, Zavattieri PD. Mechanics of chiral honeycombs architectures with phase transformations. J Appl Mech 2019;86:111014.
[42] Wu L, Xi X, Li B, Zhou J. Multi-stable mechanical structural materials. Adv Eng Mater 2018;20:1700599.
[43] Lv W, Li D, Ren X. A self-recoverable negative stiffness metamaterial with enhanced bearing and energy dissipation capacity. Smart Mater Struct 2024;33: 025035.
[44] Kappe K, Wahl JP, Gutmann F, Boyadzhieva SM, Hoschke K, Fischer SC. Design and manufacturing of a metal-based mechanical metamaterial with tunable damping properties. Materials 2022;15:5644.
[45] Chen S, Lian X, Zhu S, Li M, Wang B, Wu L. A re-usable negative stiffness mechanical metamaterial composed of Bi-material systems for high energy dissipation and shock isolation. Compos Struct 2023;322:117366.
[46] Pechac JE, Frazier MJ. Metamaterial design strategy for mechanical energy absorption under general loading. Extr Mech Lett 2022;51:101580.
[47] Auricchio F, Bacigalupo A, Gambarotta L, Lepidi M, Morganti S, Vadala F. A novel layered topology of auxetic materials based on the tetrachiral honeycomb microstructure. Mat & Des 2019;179:107883.
[48] Yang TY, Xu HC, Tobber L. Mechanism and experimental validation of innovative self-centering conical friction damper. Struct Cont Health Monit 2020;27:e2609.
[49] Wang Y, Zeng B, Zhou Z, Xie Q. Hysteretic and seismic performance of dual self-centering variable friction damper braces. Soil Dynam Earthquake Eng 2021;147: 106774.
[50] Veismoradi S, Yousef-beik SMM, Zarnani P, Quenneville P. Development and parametric study of a new self-centering rotational friction damper. Eng Struct 2021;235:112097.
[51] Hamzehei R, Bodaghi M, Iglesias Martinez JA, Ji Q, Ulliac G, Kadic M, Wu N. Parrot beak-inspired metamaterials with friction and interlocking mechanisms 3D/ 4D printed in micro and macro scales for supreme energy absorption/dissipation. Adv Eng Mater 2023;25:2201842.
[52] Fu K, Zhao Z, Jin L. Programmable granular metamaterials for reusable energy absorption. Adv Funct Mater 2019;29:1901258.
[53] Garland AP, Adstedt KM, Casias ZJ, White BC, Mook WM, Kaehr B, Bradley HJ, Lester BT, Leathe NS, Schwaller E, Boyce BL. Coulombic friction in metamaterials to dissipate mechanical energy. Extr Mech Lett 2020;40:100847.
[54] Gambarotta L, Lagomarsino S. A microcrack damage model for brittle materials. Int J Solids Struct 1993;30:177–98.
[55] Jeong E, Calius E, Ramezani M. Design and analysis of a 3D frictional mechanical metamaterial for efficient energy dissipation. Adv Mater Technol 2024:2400614.
[56] McCrary A, Hashemi MS, Sheidaei A. Programmable bidirectional mechanical metamaterial with tunable stiffness and frictional energy dissipation. Adv Theory Simul 2022:2200135.
[57] Patil S, Ganzenmüller G, Gutmann F, Hoschke K, Hiermaier S. The auxetic friction cell: towards programming strain rate dependency and energy dissipation into mechanical metamaterials. Mater Today Commun 2023;36:106725.
[58] Li T, Li Y. 3D tiled auxetic metamaterial: a new family of mechanical metamaterial with high resilience and mechanical hysteresis. Adv Mat 2024:2309604.
[59] Lv W, Li D. A metamaterial with enhanced effective stiffness and negative Poisson's ratio for frictional energy dissipation. European Journal Mechanics-A/Solids 2024; 107:105390.
[60] Lv W, Yu P, Li D. An energy dissipation metamaterial based on Coulomb friction and vibration. Int J Mech Sci 2024;263:108764.
[61] Prall D, Lakes RS. Properties of chiral honeycomb with a Poisson ratio of -1. Int J Mech Sci 1997;39:305–14.
[62] Spadoni A, Ruzzene M. Elasto-static micropolar behavior of a chiral auxetic lattice. J Mech Phys Sol 2012;60:156–71.
[63] Liu XN, Huang GL, Hu GK. Chiral effect in plane isotropic micropolar elasticity and its application to chiral lattices. J Mech Phys Solids 2012;60:1907–21.
[64] Bacigalupo A, Gambarotta L. Homogenization of periodic hexa-and tetra-chiral cellular solids. Comp Struct 2014;116:461–76.
[65] Bacigalupo A, Gambarotta L. Simplified modelling of chiral lattice materials with local resonators. Int J Sol Struct 2016;83:126–41.
[66] Bacigalupo A, Diana V, Gambarotta L. Energy absorbing multilayered self-recovering metamaterials with chiral topology. Int J Sol Struct 2023;273:112213.
[67] Podio-Guidugli P, Virga EG. Analytical thermodynamics. J Elast 2023;153: 787–812.

[68] Hackl K, Svoboda J, Fischer FD. On the coupling of Hamilton's principle and thermodynamic extremal principles. J Mech Phys Sol 2024:105633.
[69] De Souza Neto EA, Peric D, Owen DRJ. Computational methods for plasticity: theory and applications. John Wiley & Sons; 2011.
[70] Bacigalupo A, Badino P, Diana V, Gambarotta L. Overall constitutive properties of stratified lattices with alternating chirality. Philosoph Trans A 2024;382(2279): 20230355.
[71] Diana V, Bacigalupo A, Gambarotta L. Continuum-molecular modeling of planar micropolar media: Anisotropy, chiral properties and length-scale effects. Int J Solids Struct 2024;295:112810.
[72] Chen Y, Liu XN, Hu GK, Sun QP, Zheng QS. Micropolar continuum modelling of bi-dimensional tetrachiral lattices. Proc Royal Soc A: Math, Phy Eng Sci 2014;470: 20130734.
[73] Ashby MF. Materials selection in mechanical design. Butterworth; 2011.